AGU ADVANCING EARTH AND SPACE SCIENCE

JGR Space Physics

RESEARCH ARTICLE
10.1029/2021JA029335

Key Points:

- Gravity Field and Steady-State Ocean Circulation Explorer thermospheric traveling atmospheric disturbances in austral winter are mainly induced by orographic waves during geomagnetic quiet time
- Medium and large scale traveling atmospheric disturbances in Challenging Minisatellite Payload create a bipolar distribution in austral winter quiet time
- Traveling atmospheric disturbances during geomagnetic activities are likely caused by auroral generated gravity wave

Correspondence to:
S. Xu,
shuang.xu@my.hamptonu.edu

Citation:
Xu, S., Vadas, S. L., & Yue, J. (2021). Thermospheric traveling atmospheric disturbances in austral winter from GOCE and CHAMP. *Journal of Geophysical Research: Space Physics*, *126*, e2021JA029335. https://doi.org/10.1029/2021JA029335

Received 12 MAR 2021
Accepted 17 AUG 2021

Thermospheric Traveling Atmospheric Disturbances in Austral Winter From GOCE and CHAMP

Shuang Xu[1], Sharon L. Vadas[2], and Jia Yue[3,4]

[1]Department of Atmospheric and Planetary Sciences, Hampton University, Hampton, VA, USA, [2]Northwest Research Associates, Boulder, CO, USA, [3]Physics Department, Catholic University of America, Washington, DC, USA, [4]NASA Goddard Space Flight Center, Greenbelt, MD, USA

Abstract In this study, we analyze the thermospheric density data provided by the Gravity Field and Steady-State Ocean Circulation Explorer during June–August 2010–2013 at ∼260 km altitude and the Challenging Minisatellite Payload during June–August 2004–2007 at ∼370 km altitude to study high latitude traveling atmospheric disturbances (TADs) in austral winter. We extract the TADs along the satellite tracks from the density for varying *Kp*, and linearly extrapolate the TAD distribution to $Kp = 0$; we call these the geomagnetic "quiet time" results here. We find that the quiet time spatial distribution of TADs depends on the spatial scale (along-track horizontal wavelength λ_{track}) and altitude. At $z \sim 260$ km, TADs with $\lambda_{track} \leq 330$ km are seen mainly around and slightly downstream of the Southern Andes-Antarctic region, while TADs with $\lambda_{track} > 800$ km are distributed fairly evenly around the geographic South pole at latitudes ≥60°S. At $z \sim 370$ km, TADs with $\lambda_{track} \leq 330$ km are relatively weak and are distributed fairly evenly over Antarctica, while TADs with $\lambda_{track} > 330$ km make up a bipolar distribution. For the latter, the larger size lobe is centered at ∼60°S, and is located around, downstream and somewhat upstream of the Andes/Antarctic Peninsula, while the smaller lobe is located over the Antarctic continent at 90°–150°E. We also find that the TAD morphology for $Kp \geq 2$ and $\lambda_{track} > 330$ km depends strongly on geomagnetic activity, likely due to auroral activity, with greatly enhanced TAD amplitudes with increasing *Kp*.

1. Introduction

Atmospheric gravity waves (GWs) propagate in the Earth's atmosphere and can be depicted by linear wave theory. They are launched from atmospheric phenomena such as jet stream adjustments and wind flow over mountains (Alexander et al., 1995; Becker & Vadas, 2018; Choi et al., 2007; Chun & Kim, 2008; Heale, Bossert, et al., 2020; Heale, Lund, & Fritts, 2020; Heale et al., 2019; Holton & Alexander, 1999; Lane et al., 2003; X. Liu et al., 2014; Sentman et al., 2003; Snively, 2013; Taylor & Hapgood, 1988; Vadas & Becker, 2018). Tropospheric deep convection such as thunderstorms and tropical cyclones are also common sources for GWs worldwide (Dewan et al., 1998; Fritts & Alexander, 2003; Hoffmann & Alexander, 2010). Additionally, GWs are created in the lower thermosphere at high latitudes from the aurora (Hickey & Cole, 1988; Hocke & Schlegel, 1996; Richmond, 1978). GWs are important for the transfer of energy and momentum from the lower to the upper atmosphere. Their propagation and breaking (Lindzen, 1981), dissipation (Vadas & Liu, 2009), viscous damping (Pitteway & Hines, 1963; Vadas, 2007), interaction with ionospheric plasma (Nicolls et al., 2014; Vadas & Nicolls, 2009) and secondary/tertiary generation (Vadas & Becker, 2019) make GWs play a key role in driving the atmosphere out of the radiative balance and changing the mean flow and temperature. This significantly affects the atmospheric circulation, wind and temperature structures. It also creates significant variability in the thermosphere and ionosphere.

Mountain waves (MWs) are excited when wind flows over mountains or orography. Because MWs have nearly zero phase speed, they break in the stratosphere or mesosphere where the stratospheric eastward wind reverses direction. This breaking process excites several types of secondary GWs. The first type of waves are created from the nonlinear interactions associated with wave breaking (e.g., Heale, Bossert, et al., 2020; Satomura & Sato, 1999). The second type is generated from the accelerations and heatings created from the deposition of momentum and energy into the background flow (Becker & Vadas, 2018; Vadas, 2013; Vadas & Becker, 2019; Vadas & Liu, 2009, 2013; Vadas et al., 2003, 2014). Because the second type of secondary GWs typically have larger horizontal phase speeds, horizontal wavelengths, and vertical wavelengths, many can propagate to the mesosphere and lower thermosphere (MLT) region before dissipating. This dissipation process excites so-called tertiary GWs having even larger horizontal phase speeds, thereby enabling them to propagate well into the thermosphere (Vadas & Becker, 2019). Recent modeling studies have found that these tertiary GWs can propagate to $z \sim 200$–450 km (Becker & Vadas, 2020). Thus, the GWs in the thermosphere can be described as a mixture of GWs "from below" (e.g., originally from orography via multi-step vertical coupling) and "from above" (e.g., from the aurora).

It was thought for many decades that GWs in the thermosphere with periods less than an hour and horizontal phase speeds less than 250 m/s were from below and that GWs with horizontal phase speeds >250 m/s were from auroral processes (e.g., Georges, 1968; Hocke & Schlegel, 1996; Waldock & Jones, 1986). However, recent modeling studies have shown that secondary GWs from deep convection (Vadas & Liu, 2009, 2013) and tertiary GWs from MW breaking (Vadas & Becker, 2019) (both generated in the thermosphere) can have horizontal phase speeds much larger than 250 m/s. Additionally, observational/modeling studies have shown that some of the secondary GWs from deep convection (generated in the thermosphere) have horizontal phase speeds of 100–250 m/s (Vadas & Azeem, 2020; Vadas & Crowley, 2010). Therefore, the horizontal phase speed of a GW from deep convection cannot be used to determine if it is a primary or secondary GW without detailed study.

In the thermosphere, GWs have been observed for decades in the ionosphere using ground-based instruments, because GWs induce traveling ionospheric disturbances from neutral-ion collisions (Azeem et al., 2015, 2017; Crowley et al., 1987; Djuth et al., 1997, 2004; Hocke & Schlegel, 1996; Hocke et al., 1996; Nicolls et al., 2014; Ogawa et al., 1987; Oliver et al., 1997; Vadas & Nicolls, 2009; Xu et al., 2019). In addition, thermospheric GWs have been observed from satellite measurements, such as the Atmosphere Explorer, Dynamics Explorer-2, Satellite Electrostatic Triaxial Accelerometer Experiment, Gravity Field and Steady-State Ocean Circulation Explorer (GOCE) and the Challenging Minisatellite Payload (CHAMP) satellites (e.g., Bruinsma & Forbes, 2008; Forbes, 1995; Forbes et al., 2016; Hedin & Mayr, 1987; Innis & Conde, 2002; H. X. Liu et al., 2017; Mayr et al., 1990; Park et al., 2014; Trinh et al., 2018). Because these measurements are in-situ, only the along-track horizontal wavelengths, λ_{track}, can be directly determined. However, the GW dissipative polarization and dispersion relations can be used to determine the intrinsic parameters of these GWs (such as horizontal wavelength and direction of propagation) (Vadas & Nicolls, 2012; Vadas et al., 2019). Many researchers have observed a traveling atmospheric disturbance (TAD) hotspot in the GOCE and CHAMP density perturbations over the quiet time wintertime Southern Andes (Forbes et al., 2016; Park et al., 2014; Trinh et al., 2018). The TADs analyzed in these studies have along-track wavelengths of less than ~600–700 km. The origin of these GWs was considered a mystery, however, because MWs have very slow horizontal phase speeds and therefore would dissipate very rapidly in the thermosphere from viscosity if indeed they could propagate there before breaking (Vadas, 2007). A recent quiet time case study found that most of these observed hotspot GOCE TADs were likely tertiary GWs created in the thermosphere from the dissipation of secondary GWs excited by MW breaking (Vadas et al., 2019). Indeed, reverse ray tracing found that most of those GOCE GWs could not propagate below the mesopause.

A recent study using the HIgh-Altitude Mechanistic general Circulation Model (HIAMCM) has reproduced, for the first time from a model, the occurrence of a wintertime hotspot of thermospheric GWs over the Southern Andes-Antarctic Peninsula which only include GWs from below (Becker & Vadas, 2020). (HIAMCM is a high-resolution GW-resolving model which simulates the atmosphere up to $z \sim 450$ km. This model does not include ion chemistry, geomagnetic disturbances or energetic particle precipitation.) They found that those GWs with $\lambda_H \leq 330$ km create a distinct hotspot over the Southern Andes-Antarctic Peninsula. In addition, they found that those GWs with $\lambda_H > 800$ km do not contribute to this hotspot, but instead create a fairly diffuse GW "ring" around Antarctica, with the largest amplitude being on the side of Antarctica that is opposite to the Southern Andes. They argued that this ring occurs because those GWs with larger horizontal wavelengths λ_H typically have much larger periods, and therefore propagate much closer to the horizontal. In order for these GWs to propagate to $z \sim 400$ km, they would simultaneously propagate thousands or tens of thousands of km horizontally. Those GWs with $\lambda_H \leq 330$ km, on the other hand, typically have much smaller periods, and therefore propagate much closer to the vertical; this is why these latter GWs create a hotspot over the Southern Andes-Antarctic Peninsula. This modeling study is inspiring because it shows that larger-scale, larger-period GWs observed in the upper thermosphere might be from below (in this case, ultimately from MW breaking), rather than from geomagnetic activity. However, grouping TADs over the Southern Andes and Antarctic continent within different horizontal scale bins has not yet been done for GOCE and CHAMP satellite observations.

The objective of this paper is to determine the quiet time distributions of TADs as a function of λ_{track} and altitude in the winter Southern Hemisphere from GOCE and CHAMP satellite data. In doing so, we also examine the TAD distributions as functions of Kp in order to determine how these distributions are related to geomagnetic activity. This paper is arranged as follows. In Section 2, we describe the satellite datasets we use, introduce a new method to extract TADs along the satellite track, and describe how we process the data. The climatological TAD results as a function of the Kp index are shown in Section 3. In Section 4, we extrapolate our results to $K\mathrm{p} = 0$ to determine the quiet time TAD distributions. We also investigate how geomagnetic activity affects the TAD distributions in relation to the geomagnetic pole. Our conclusions are provided in Section 5. Appendix A contains details of our new wave extraction method from along-track satellite measurements.

2. Satellites and Datasets

2.1. GOCE and CHAMP

The GOCE satellite was an European Space Agency (ESA) geodynamics and geodetic mission. The GOCE was in a near sun-synchronous orbit from March 17, 2009 until it reentered the Earth's atmosphere on November 11, 2013. The satellite was in an unusually low orbital altitude of ∼250–290 km with an inclination of ∼96.7°(H. X. Liu et al., 2017). To maintain this low altitude against high drag forces for 4–5 years, the satellite used an ion thruster assembly that acted aligned to the orbit direction (Doornbos et al., 2009). Note that the adjustments made by this thruster cause increased data uncertainties, which can affect the quality of the density and wind data. The GOCE's local solar time (LST) drifted slowly from 18:00 to 19:40 at the ascending node (or from 06:00 to 07:40 at the descending node) during its life span (Doornbos, 2016, Figure 2.1). The GOCE carried a payload Electrostatic Gravity Gradiometer with a noise level of 10^{-12} m s^{-2} Hz$^{-1/2}$, which consisted of six highly accurate accelerometers. The thruster data is used to derive the acceleration (including the drag force). The density and cross track wind are determined using a satellite geometry model with radiation pressure removed (Doornbos et al., 2013). In this research, we use the GOCE data set version 1.5 provided by ESA (Doornbos, 2016).

The CHAMP mission was managed by the GFZ (GeoForschungsZentrum, or Geo-research Centre). CHAMP was launched on July 15, 2000 and re-entered on September 19, 2010. This mission was dedicated to measure gravity and the Earth's magnetic field to high precision. CHAMP was in a near-circular orbit with an inclination of ∼87°, and its ascending and descending nodes covered all (24-h) local solar time (LST) about every 4 months (Bruinsma & Forbes, 2008). The altitude of the satellite was $z \sim 450$ km at the beginning and gradually decreased to $z \sim 260$ km in August 2010. Although CHAMP's altitude decreased by over 100 km in 2001–2009, the background density at CHAMP altitudes was very stable during this time due to the contraction of the thermosphere as the Sun transitioned from solar max to extreme solar min (see Section 2.2). CHAMP was equipped with a STAR (Space Three-axis Accelerometer for Research mission) accelerometer. Note that CHAMP's measurements were less precise than the GOCE's. Moreover, the X-axis sensor of the sole accelerometer (parallel to the Z-axis of the body system, nominally pointed toward the satellite's nadir) was less sensitive than its sensors along the other two axes. Nevertheless, the sensors along the other two axes still had a resolution $<3 \times 10^{-9}$ m s^{-2} Hz$^{-1/2}$ (Doornbos et al., 2009; Touboul et al., 2012), which is adequate for the purpose of thermospheric TAD analysis. According to Doornbos et al. (2013), the approach for retrieving the density and cross track wind from the CHAMP data set is essentially same as that from the GOCE data set.

2.2. Data Description

In Figure 1a, we show the average Kp index and the Solar Radio Flux at 10.7 cm (F10.7) data using an 81-day sliding window to obtain climatology values. In Figure 1b, we show the average background density from CHAMP and GOCE for only the southern polar region (90°S–60°S). (Note that the thermosphere neutral density in the northern polar region is often ∼3 times larger than that in the southern polar region

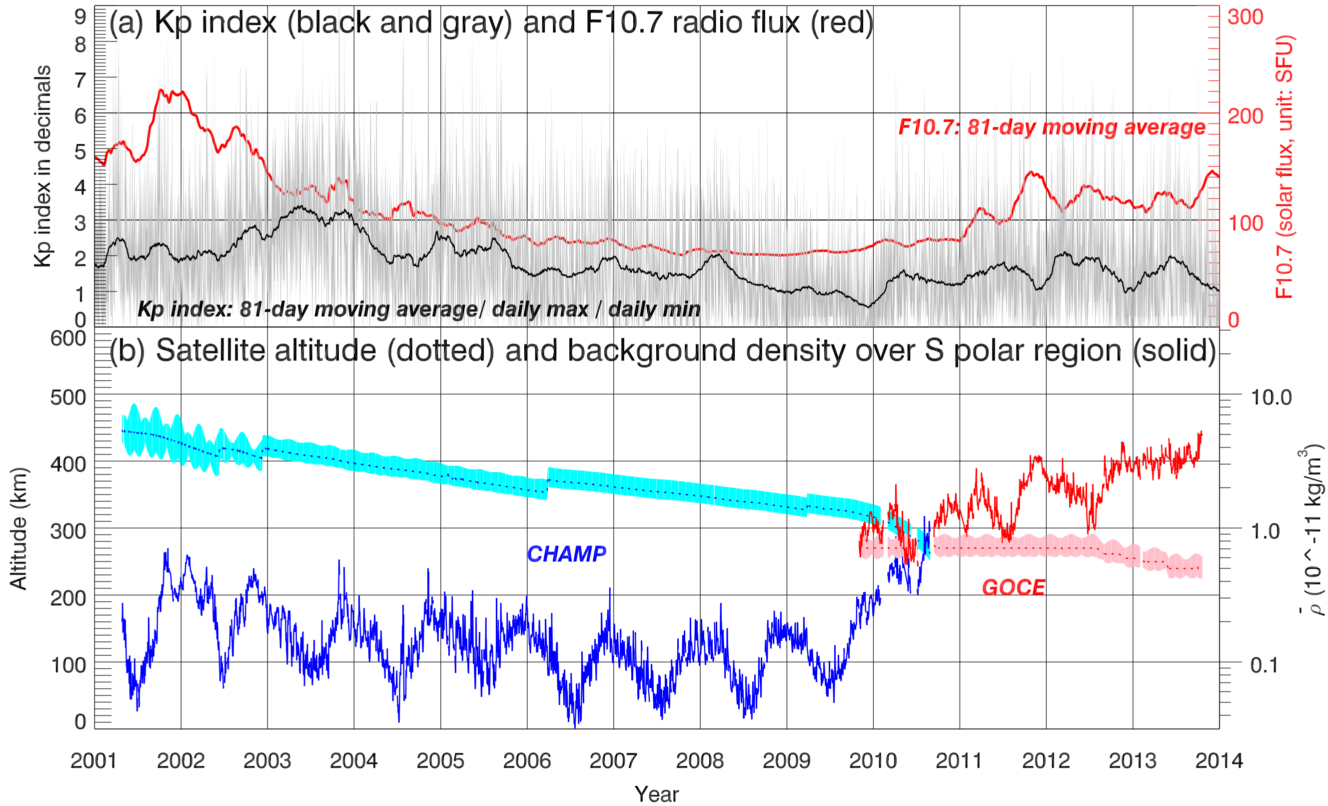

Figure 1. (a) The *K*p index and Solar F10.7. The black curve shows the average *K*p index using an 81-day sliding window. The gray curve shows the daily maximum and daily minimum *K*p values. The red curve shows the average F10.7 data using an 81-day sliding window. (b) The left *y*-axis scales altitude information: The blue (red) dotted line shows the daily mean altitude of CHAMP (GOCE), while the cyan (pink) shading shows the daily maximum & minimum altitudes of CHAMP (GOCE). The right *y*-axis scales the background density over the southern polar region for CHAMP (solid blue line) and GOCE (solid red line). The term "S polar region" includes data with $-90° \leq$ latitude $\leq -60°$. Note that CHAMP and GOCE only overlapped during 2009–2010.

around June solstice.) Figure 1b also shows the altitudes of the GOCE and CHAMP satellites. Despite the decreasing altitude of the CHAMP satellite from 2001 to 2009, the background in-situ density at CHAMP altitudes is roughly constant, with only a slight decrease in time. This is caused by the contraction of the thermosphere and the accompanying decrease of the thermospheric density at a given altitude due to the decreasing thermospheric temperature as the Sun transitioned from solar maximum (2001) to solar minimum (2009) during the second half of Solar Cycle (SC) 23 and the beginning of SC24.

In this paper, we focus on the GOCE density data during June–August 2010–2013 and the CHAMP density data during June–August 2004–2007, because the satellites were at relatively stable altitudes during those periods. The average altitude and corresponding standard deviation of the data points during these times are ~260.3 ± 16.6 km for GOCE and ~368.8 ± 15.1 km for CHAMP. Normally, the GOCE and CHAMP data sets provide 1 data point every 10 s, and the *K*p index is provided every 3 h. Figure 2 shows histograms of the number of CHAMP and GOCE data points as functions of the *K*p from $Kp = 0$ to $Kp = 9$. Most of the data points occur for $Kp = 0.3$ to 3.3. Additionally, there are few data points for $Kp > 4$, making it more difficult to characterize the dependence of TAD distributions on stronger geomagnetic activity.

The LST of GOCE is relatively stable, while it changes regularly for CHAMP (from 0 to 24 LST about every 4 months). Therefore, the data points from CHAMP are reduced significantly when analyzing a limited LST range. For example, if we focus on the CHAMP data during 9–18 LST, only ~37.5% of total data points in Figure 2 are useable for the analysis.

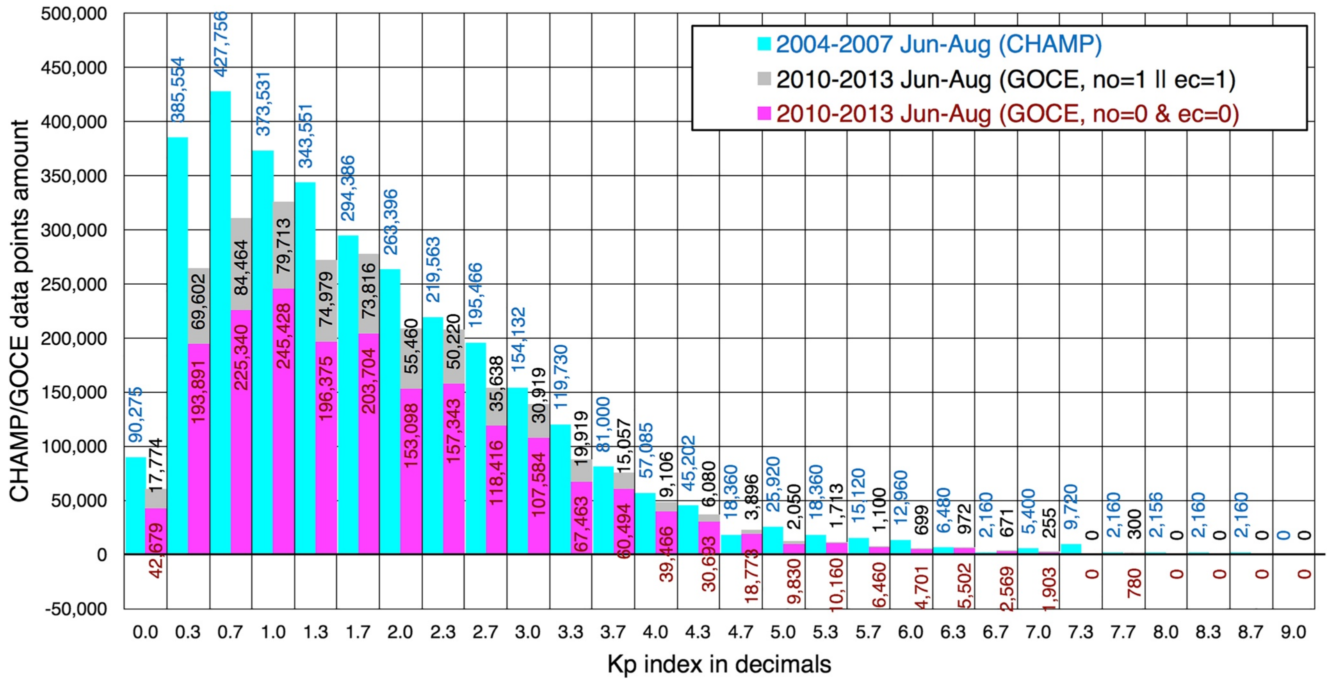

Figure 2. Histograms of the number of CHAMP data points during June–August 2004–2007 (cyan) and the number of GOCE data points during June–August 2010–2013 (gray plus magenta) as a function of the *K*p index. For the GOCE data, "no" and "ec" denotes "noise" and "eclipse," respectively. "no = 1 || ec = 1" means the GOCE data was "possibly affected by increased noise from Ion Thruster Assembly or possibly affected by eclipse transition," and "no = 0 & ec = 0" means the GOCE data quality was OK. Note that the CHAMP data set does not provide data quality flags such as "no" or "ec.".

2.3. Data Processing From the GOCE and CHAMP Thermospheric Density Data Sets

We extract TADs according to their along-track horizontal wavelengths, λ_{track}, from the GOCE and CHAMP thermospheric density data sets. In this study, we bin the results in three λ_{track} ranges: λ_{track} = 160–330 km, λ_{track} = 330–800 km, and λ_{track} = 800–2,100 km. In order to more-accurately bin the TADs into these precise λ_{track} ranges, we utilize a new TAD extraction method here. To extract TADs within a given λ_{track} range from a segment of satellite data, we apply a quasi-box shaped Butterworth band-pass filter (assembled from two high-order Butterworth filters) to divide the time-dependent in-situ density (ρ) into the background density $\bar{\rho}$ plus the perturbation density ρ', where the perturbations have λ_{track} within the desired range. Details of this wave extraction method are provided in Appendix A. We then create a map of the Standard Deviation of the TAD distribution (TAD is defined as $\rho'/\bar{\rho}$) in 5° by 5° longitude-latitude bins. We also denote the term "Standard Deviation of TAD" as SD(TAD) or STDDEV$\left(\rho_i'/\bar{\rho}_i\right)$ or $\sqrt{1/(N-1)\sum_i\left(\rho_i'/\bar{\rho}_i\right)^2}$, where "i" denotes each along-track data point that occurs in each 5° by 5° bin and "N" stands for the total amount in each bin.

3. Results

3.1. GOCE TADs

Since each GOCE data point is associated with a specific *K*p index, binning of the along-track TADs according to their associated *K*p values can be used to examine the influence of the *K*p index, or geomagnetic activity, on TAD variability at the GOCE altitudes, that is, ~250–260 km. Figure 3 shows the global climatology of SD(TAD)s at the GOCE altitudes. Each map contains 72 × 36 bins, with 90% of the bins having ≥76 ($0 \le Kp \le 0.3$), ≥46 ($Kp = 2.0$) and ≥39 ($4.0 \le Kp \le 7.7$) data points, respectively. Figure 3a shows the TAD amplitude distribution for the small-medium-scale TADs for $0 \le Kp \le 0.3$. The TAD activity is moderate over (summertime) North America and East Asia, which are consistent with the stratospheric GW activity in Figures 6c and 7c of Hoffmann et al. (2013). This high TAD activity during the summertime at mid-latitudes is related to deep convection. A close examination of Figure 3a indicates increased activity over North

10.1029/2021JA029335

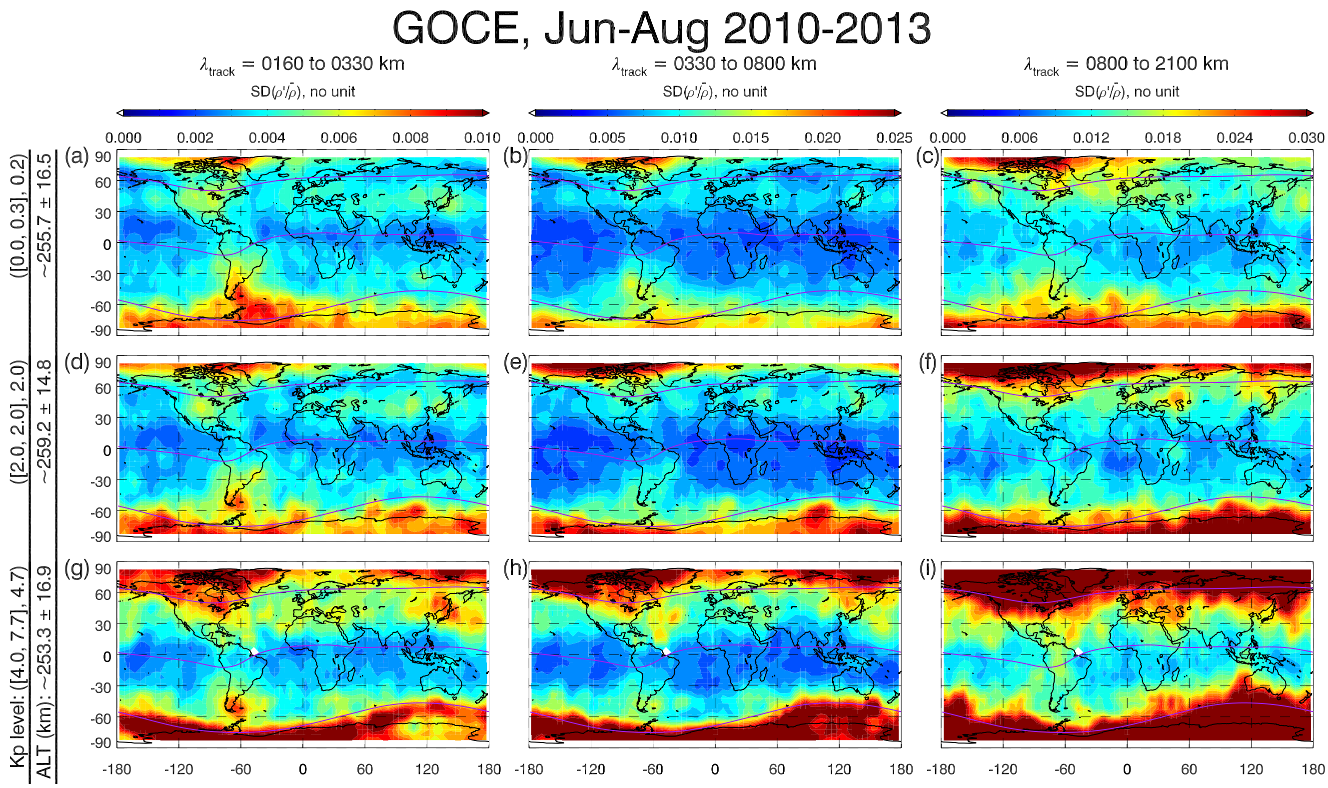

Figure 3. Global distribution of GOCE SD(TAD) or $\sqrt{1/(N-1)\sum_i\left(\rho_i'/\bar{\rho}_i\right)^2}$, which is the standard deviation of the relative density perturbations of all GOCE events in each 5° × 5° bin. This includes all GOCE data during June–August 2010–2013 with "no = 0 & ec = 0." The first row (from left to right) shows the SD(TAD) distribution for small-medium-scale traveling atmospheric disturbances (TADs) with λ_{track} = 160–330 km, medium-scale TADs with λ_{track} = 330–800 km, and large-scale TADs with λ_{track} = 800–2,100 km, respectively, for $0 \le Kp \le 0.3$ (median $Kp = 0.2$). The second and third row show the same as in the first row but for $Kp = 2.0$ (median $Kp = 2.0$) and $4.0 \le Kp \le 7.7$ (median $Kp = 4.7$), respectively. The average altitude and corresponding standard deviation for the GOCE data points are ~255.7 ± 16.5 km, ~259.2 ± 14.8 km, and ~253.3 ± 16.9 km for rows 1, 2, and 3, respectively. The maps in the panels are smoothed with a boxcar average of 3 × 3 bins centered at each 5° × 5° map bin.

America, East Asia, and West Europe, in the order of smaller amplitudes. It is similar to the three-peak longitudinal structure reported in reported by H. X. Liu et al. (2017, Figure 1, June solstice), who also used the GOCE measurements. At mid- to high-latitudes, high TAD activity is clearly seen above and somewhat east (downstream) of the Southern Andes-Antarctic Peninsula region at 40°–80°S. This TAD hotspot agrees with recent HIAMCM results (Becker & Vadas, 2020), who found that GWs with small-medium-scales created a hotspot over and somewhat east of the Southern Andes-Antarctic Peninsula region; these authors found that this hotspot was composed of tertiary GWs that ultimately resulted from mountain-wave breaking over the Southern Andes and Antarctic Peninsula at z = 200–380 km (their Figures 12f, 12i, and 12l).

From the first column in Figure 3, this TAD hotspot remains as Kp increases, although the TAD amplitudes poleward of 60°S in the Antarctic region increase as Kp increases. This shows that even in the presence of geomagnetic activity, waves from below (i.e., tertiary GWs from mountain wave breaking) are still present and are important components of the variability at $z \sim 260$ km. Figure 4 shows the same TADs as in Figure 3, except that the maps are azimuthal equidistant projections centered on the geographic South pole. From the first column in Figure 4, we see that (a) the TAD hotspot over the Southern Andes-Antarctic region remains with increasing Kp, and (b) the TAD amplitudes become stronger as Kp increases. This second point suggests that small-medium scale TADs are increasingly created as geomagnetic activity becomes stronger. Additionally, it is clear from Figure 4g (for $4.0 \le Kp \le 7.7$) that the TAD distribution forms a ring-like structure around Antarctica at geomagnetic latitudes of −60° to −75°. This ring-shaped distribution overlaps with (and is slightly broader than) the location of the auroral oval, of which the equatorward edge to poleward edge are at geomagnetic latitudes of ~−60° to ~−75° when the magnetic disturbance level is

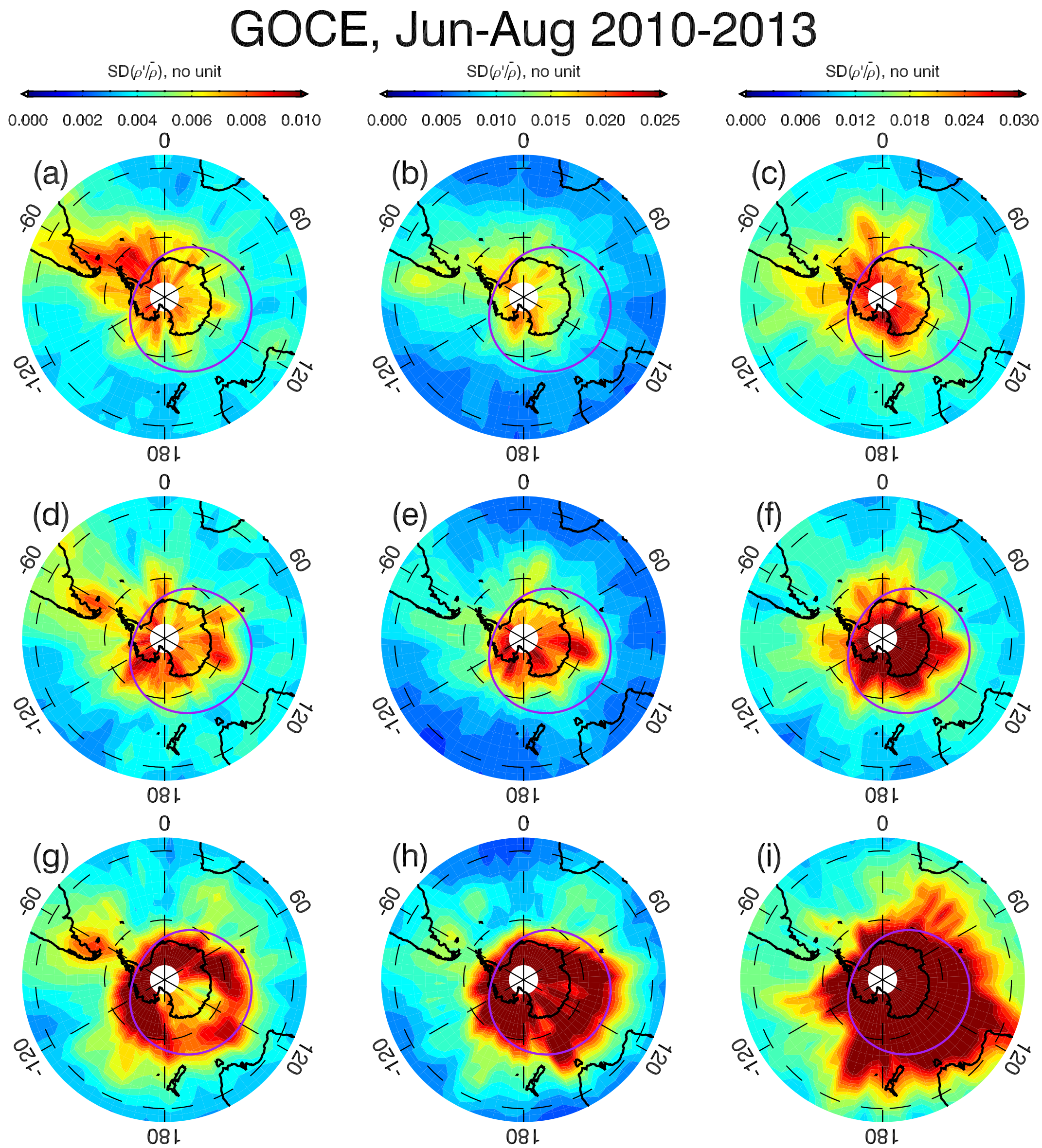

Figure 4. The same as in Figure 3 but for an azimuthal equidistant projection centered on the geographic South pole. The purple ring depicts the geomagnetic latitude of −60°.

relatively high (Feldstein & Galperin, 1985) (see Section 4). Since GWs are created by auroral heating at $z \sim 120$–150 km (Hocke & Schlegel, 1996), Figure 4g shows that auroral heating creates small-medium-scale GWs. This result is consistent with the fact that the TAD distribution overlaps well with the aurora oval, since small-medium-scale GWs tend to have medium to high frequencies, and therefore cannot propagate very far horizontally as they propagate vertically in the thermosphere (Vadas, 2007).

The distribution of TADs with $\lambda_{\mathrm{track}} = 330$–800 km, as shown in the second columns of Figures 3 and 4 (i.e., the medium-scale along-track TADs) is similar to that for the small-medium-scale TADs, except that the hotspot over the Southern Andes-Antarctic Peninsula is quite diffuse and has a much smaller amplitude. Instead, the quiet time TAD activity is concentrated around the geographic South pole. Although more diffuse, this weak hotspot over the Southern Andes does remain as *K*p increases, however. Note that for larger geomagnetic activity (Figure 4h), the TAD distribution overlaps with the area enclosed by the aurora oval, although it is smeared out horizontally as compared to Figure 4g. This is because the medium-scale GWs excited by the aurora tend to have smaller frequencies and therefore propagate further horizontally as they propagate vertically in the thermosphere.

As compared to the TADs with smaller λ_{track}, the large-scale along-track TADs with λ_{track} = 800–2,100 km shown in the third column of Figures 3 and 4 have a different distribution of TADs in the southern polar region. Most importantly, there is no apparent TAD hotspot over the Southern Andes-Antarctic Peninsula region during quiet time ($0 \le Kp \le 0.3$, Figures 3c and 4c); instead, the TAD distribution is centered on the geographic South pole and is concentrated over the Antarctic continent and the circumpolar ocean surrounding Antarctica. This result agrees well with the model results of Becker and Vadas (2020), who found that tertiary GWs from mountain wave breaking over the Southern Andes-Antarctic Peninsula with large horizontal wavelengths λ_H propagated large distances horizontally before reaching z = 200–380 km because of their large periods (their Figures 12d, 12g, and 12j). However, they also found that the GW amplitudes were significantly smaller for GWs at 60°W–40°E at $z \sim$ 200–300 km, which is downstream of the Southern Andes-Antarctic Peninsula; the dearth of GWs in this region is due to the large horizontal distances propagated by these lower-frequency GWs. While this is a striking feature of the model results, we do not see this in the data in Figure 4c. In fact, the opposite occurs, which is that there are many large-amplitude TADs in this region. This likely occurs because the GOCE data for this λ_{track}range also includes GWs with much smaller horizontal wavelengths λ_H, which occurs when the satellite track is nearly (but not exactly) perpendicularly aligned with the direction of propagation of a GW having a small to medium-scale λ_H (see Figure 5 in Vadas et al., 2019). These GWs with small-medium λ_H mainly have large frequencies (in order to survive dissipative damping in the thermosphere (Vadas, 2007)), which results in them propagating close to the zenith with resulting short horizontal propagation distances from their sources in the lower thermosphere.

Finally, from the third column of Figure 4, we note that the center of the TAD distribution over Antarctica in the southern polar region shifts from the geographic to the geomagnetic South pole as the Kp index increases. As above, this again suggests that these additional TADs are created from auroral heating. This shift is also accompanied by larger TAD amplitudes. Additionally, the horizontal area covered by these TADs is larger than for λ_{track} = 330–800 km, which again likely occurs because the larger-scale GWs excited by the aurora have larger periods and therefore propagate further horizontally in reaching $z \sim$ 260 km. From the first row to the third row in Figures 3 and 4, we see that the amplitudes of TADs in mid- and low-latitude regions also increase with increasing Kp indices. This can be explained by propagation of Joule heating excited GWs or TADs from high latitudes to the lower latitudes (Richmond & Roble, 1979; Schunk & Nagy, 2009, Section 12.14).

3.2. CHAMP TADs

Like GOCE, the CHAMP data is also time-dependent (one data point every 10 s). We bin the CHAMP TADs into 3 Kp groups (Kp = 0–0.3, Kp = 2.0, and Kp = 4.3–8.7) in order to investigate the influence of geomagnetic activity on the TAD variability at the CHAMP altitudes, that is, $z \sim$ 360 km. Figure 5 shows the global climatology of SD(TAD) at the CHAMP altitudes. For these maps, 90% of the 72 × 36 bins have ≥54 ($0 \le Kp \le 0.3$), ≥31 (Kp = 2.0) and ≥20 ($4.3 \le Kp \le 8.7$) data points, respectively. Since the quality of the CHAMP data is not as good as that for GOCE, the CHAMP TAD maps are smoothed using a larger running window (the average of 5° × 5° bins centered at each map bin) in Figure 5. Note that the LST of the CHAMP shifts relatively quickly and covers all LST approximately every 4 months. Therefore, in order to eliminate possible tidal variations due to different LST values, we follow the LST range chosen by Park et al. (2014), which is that only local daytime data (LST of 9–18 h) are selected to create the TAD distribution maps. It is also a way to reduce the influence from auroral activity during quiet times, since the energy flux density supplied to the auroral oval altitudes is 3–5 times higher at nighttime compared with the daytime (Feldstein & Galperin, 1985).

The first columns in Figures 5 and 6 show the distribution of the small-medium-scale along-track TADs for different Kp ranges. There is a very weak hotspot of TADs over the Southern Andes-Antarctic Peninsula region; this is similar to Figures 3 and 4, although the hotspot here has a much smaller relative amplitude and is much more diffuse at this altitude. This result, that the amplitude of the Southern Andes-Antarctic Peninsula hotspot due to GWs with small-medium scales is much smaller at CHAMP than at GOCE altitudes, is supported by model results; from Becker and Vadas (2020), the temperature variance of the small-medium

10.1029/2021JA029335

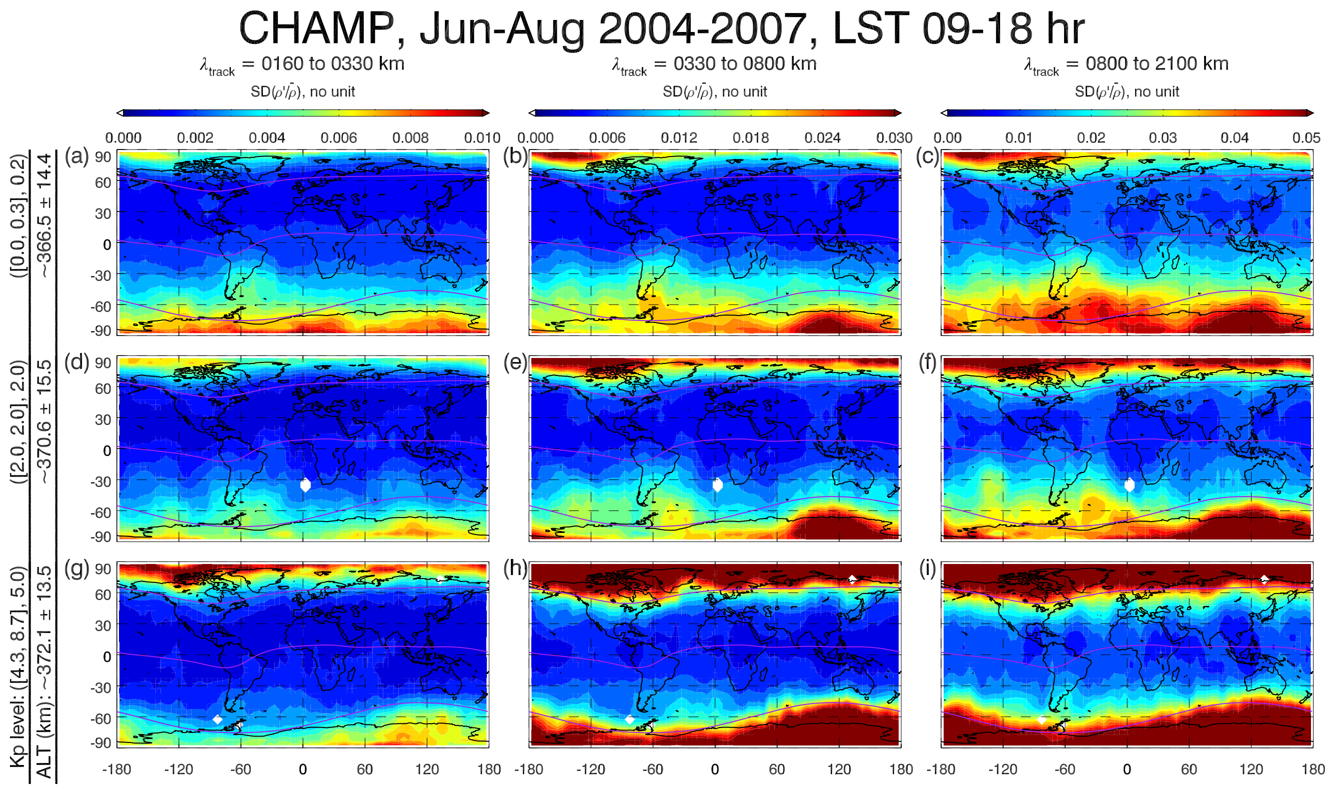

Figure 5. The same as Figure 3 but using CHAMP data during local daily time (LST 9–18 h), June–August 2004–2007. For rows 1, 2, and 3, we compute the SD(TAD)s for $0 \le Kp \le 0.3$ (median $Kp = 0.2$), $Kp = 2.0$ (median $Kp = 2.0$) and $4.3 \le Kp \le 8.7$ (median $Kp = 4.7$), respectively. The average altitude and corresponding standard deviation of the CHAMP data points are ~366.5 ± 14.4 km, ~370.6 ± 15.5 km, and ~372.1 ± 13.5 km for rows 1, 2, and 3, respectively. The maps in the panels are smoothed with a boxcar average of 5 × 5 bins centered at each 5° × 5° map bin.

hotspot GWs decreases by a factor of 10, from ~10 K^2 to ~1 K^2 from $z \sim 250$ to $z \sim 380$ km (see Figures 12f, 12i, and 12l in that work), resulting in a decrease in $\rho'/\rho \sim T'/T \sim \sqrt{10} \sim 3.2$. This is likely due to the fact that these GWs have smaller horizontal phase speeds and smaller vertical wavelengths, which causes them to succumb to molecular viscosity between these altitudes (Vadas, 2007).

As Kp increases, the amplitudes of the TADs decrease at low- and mid-latitudes. This is opposite to the GOCE results. We do not have an explicit explanation for this discrepancy, but it is possibly because that CHAMP data is less sensitive than GOCE data in density perturbation retrieval, which is due to the different capabilities of instruments onboard GOCE and CHAMP (see Section 2.1). During the quiet time ($0 \le Kp \le 0.3$), the amplitudes of the TADs around the geographic South pole are large. As Kp increases, the TADs shift gradually to the geomagnetic South pole, although with decreasing amplitudes.

In Figures 5b and 5c and 6b and 6c, the amplitudes of the quiet time medium- and large-scale along-track TADs at CHAMP altitudes are generally larger than those at GOCE altitudes (Figures 3b and 3c and 4b and 4c). This is likely due to the growth of GW amplitudes with altitude. If an upward-propagating GW is not damped by dissipative processes (such as molecular viscosity), then its amplitude $\rho'/\bar{\rho}$ will grow approximately exponentially with altitude; this growth factor is approximately $\exp\left(z/2H\right)$ in an isothermal windless and nondissipative atmosphere (Hines, 1964). Compared to the amplitudes of small-medium TADs, the amplitudes of the quiet time medium- and large-scale along-track TADs are much larger in the vicinity of the Southern Andes-Antarctica Peninsula. Although the amplitude enhancement (relative to the small-medium scale hotspot TADs in Figures 5a and 6a) is in agreement with model results (Figure 11 of Becker & Vadas, 2020), there is an excess of TADs just east of the Southern Andes-Antarctica Peninsula as compared with the model results for the medium and large λ_H GWs. As argued above for the GOCE GWs, this is likely because the medium and large-scale λ_{track}TADs also contain small-medium λ_H GWs; this would

10.1029/2021JA029335

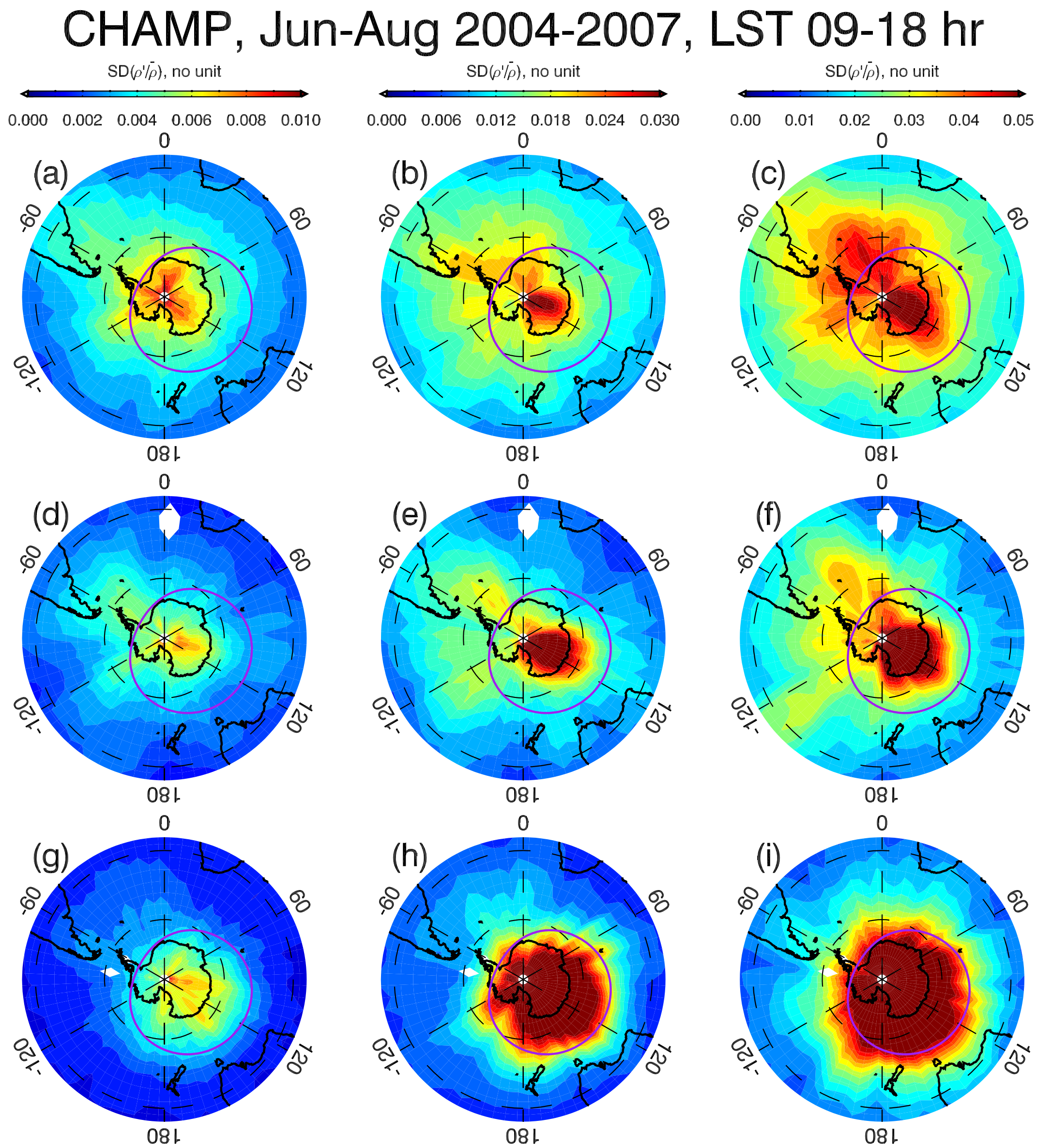

Figure 6. The same as in Figure 5 but for an azimuthal equidistant projection centered on the geographic South pole.

occur when the satellite track makes a significant angle with respect to the GW propagation direction (see description about Figure 4c in Section 3.1).

Another feature of the CHAMP results which agrees well with the model results is that there is a significant TAD hotspot maximum on the opposite side of the Antarctic continent from the Antarctic Peninsula, at 120°E (compare Figures 6b and 6c with Figure 11 of Becker & Vadas, 2020). This hotspot occurs away from the Southern Andes-Antarctica Peninsula because the large λ_H tertiary GWs propagate large distances horizontally in reaching $z \sim 360$ km, as described previously.

As *K*p increases in the second and third rows of Figures 5 and 6, the TAD amplitudes increase significantly and becomes a wide swath surrounding the geomagnetic South pole. The change of the TAD amplitudes with respect to *K*p is similar to that in the first column, but there are differences. Most notably, the amplitudes of the TADs having medium- and large-scales increases significantly (as opposed to decreasing somewhat for small-medium scales), thereby suggesting that auroral heating and geomagnetic activity create

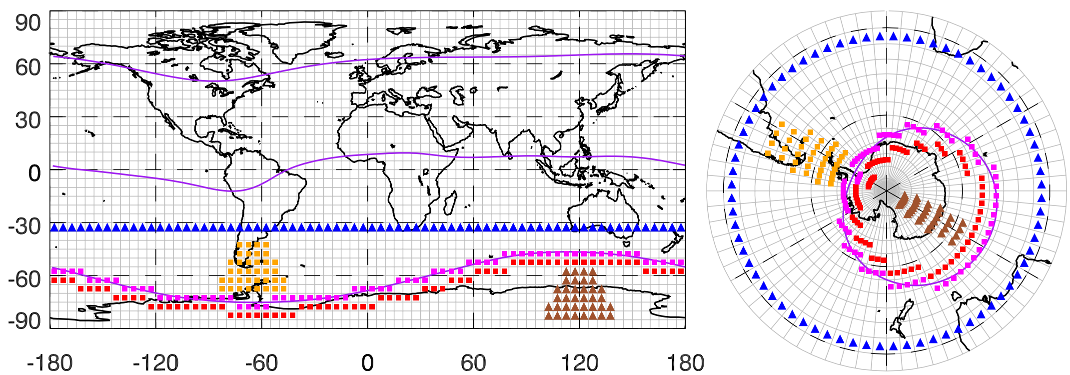

Figure 7. Five regions used for the specific linear analysis of traveling atmospheric disturbances (see Figures 8 and 10). The regions are (1) the auroral oval region: magnetic latitude ∼−65° as red squares, (2) auroral oval region: magnetic latitude ∼−60° as magenta squares, (3) Southern Andes region as orange squares, (4) Wilkes Land region as brown triangles, (5) geographic latitude of 32.5°S as blue triangles.

medium and largeλ_H GWs that are capable of surviving molecular viscosity and can propagate to CHAMP altitudes.

4. Quiet Time Results: Extrapolation to *K*p = 0

4.1. Quiet Time TADs at GOCE Altitudes

Among previous studies of thermospheric TADs during the so-called quiet time, most were based on analyses of satellite observations when $Kp < 3$ or <4 (Bruinsma & Forbes, 2008; H. X. Liu et al., 2017; Park et al., 2014; Trinh et al., 2018). However, $Kp < 3$ or <4 is not a sufficient criterion to completely remove the influence from geomagnetic activity. According to Mayr et al. (1990), the geomagnetic index is a poor measure of GW excitation mechanisms. The index is a measure of global energy deposition, while a GW is a resonance phenomenon when a local source satisfies a certain excitation condition. In this section, we introduce a new method by which to determine the quiet time TADs from GOCE and CHAMP data.

In Section 2, we binned the GOCE and CHAMP TAD results into more than 10 different *K*p ranges. The results of three of these *K*p ranges were shown in rows 1–3 in Figures 3–6. We now improve the characterization of the dependence of TADs on geomagnetic activity in order to determine the "true" quiet time results. For a given SD(TAD) map, we apply a linear Least-Squares (L-S) fitting to the SD(TAD) values in each 5° × 5° bin as a function of *K*p for $0 < Kp \leq 3$. We then extrapolate this linear fit to $Kp = 0$, and remake a SD(TAD) map using these linearly extrapolated results. This new map is then assumed to contain minimal influence from geomagnetic activity. This method is inspired by Hedin and Mayr (1987), whose Figure 7 shows the atomic oxygen density perturbations at $z = 300$ km altitude as a function of geomagnetic index and magnetic latitude in a long-wavelength band (400–4,000 km) and a short-wavelength band (40–400 km) separately. Although the longitudinal variation is not shown in their result, we show both the longitudinal and latitudinal variations here.

In order to illustrate our method, we select five specific regions, shown in Figure 7, which includes two magnetic latitudes within the auroral oval region, the Southern Andes region, Wilkes Land region, and a southern latitude strip at 32.5°S. The geomagnetic latitudes ∼−65° and ∼−60° are close to the equatorward edge of the aurora oval, the Southern Andes region is a well-known source of orographic GWs, and the geographic latitude of 32.5°S is selected as a southern mid-latitude region as a reference. We choose the Wilkes Land region because the geomagnetic pole is located near its coast.

We show the corresponding TAD results versus *K*p for the same λ_{track} ranges we considered previously for these regions in Figure 8. From the first 2 rows (Figures 8a–8f), the SD(TAD)s increase steeply when $Kp > 3.0$ for all λ_{track} ranges in the auroral oval region, thereby showing that increased geomagnetic activity does lead to an increase in TADs. From the third row (Figures 8g–8i), the SD(TAD)s is flat or slightly decreases with *K*p for $0 < Kp \leq 3$ for small-medium, medium and large-scale λ_{track} TADs in the Southern

10.1029/2021JA029335

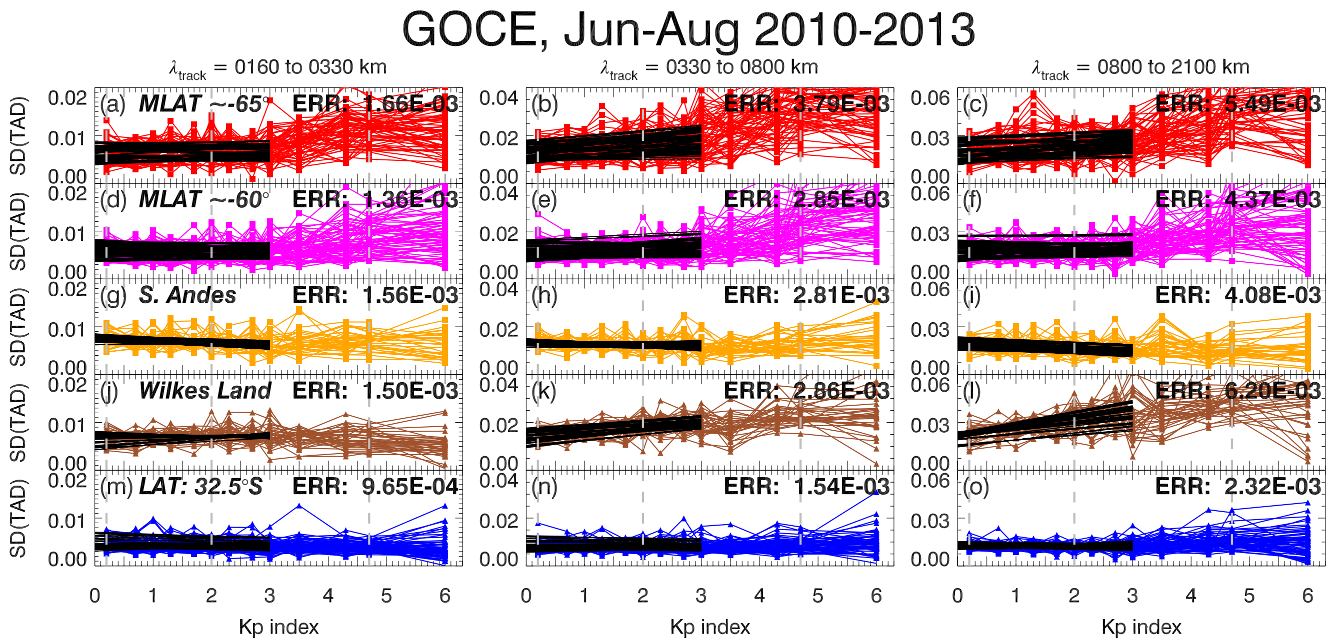

Figure 8. SD(TAD) from GOCE data during June–August 2010–2013 with "no = 0 & ec = 0." Columns 1, 2, and 3 shows SD(TAD)s with no smoothing for small-medium-scale traveling atmospheric disturbances (TADs) with λ_{track} = 160–330 km, medium-scale TADs with λ_{track} = 330–800 km, and large-scale TADs with λ_{track} = 800–2,100 km, respectively. The five rows show the results for the five regions from Figure 7 using the same symbols and colors. The black straight lines denote linear Least-Squares (L-S) fittings of each sample bin when $0 < Kp \leq 3$. The Y-intercepts of the black lines are the extrapolated SD(TAD) results at $Kp = 0$. The gray dashed vertical lines correspond to the 3 selected Kp levels in Figure 3 rows (a–c). The "ERR" (error) value in each panel shows the standard deviation of the residuals to the linear fit, which represents the error or fluctuation in the data for $0 < Kp \leq 3$.

Andes region. This is likely because most of the GWs excited by geomagnetic activity do not propagate to the Southern Andes region. The forth row (Figures 8j–8l) shows that the SD(TAD)s increase substantially for medium and large-scale λ_{track} TADs over the Wilkes Land region when $0 < Kp \leq 3.0$. However, the SD(TAD)s only increases slightly with $0 < Kp \leq 3$ for small-medium-scale λ_{track} TADs. This is either because small-medium-scale GWs are not typically excited by the aurora, or that they are dissipated by molecular viscosity before reaching GOCE's altitude. The fifth row (Figures 8m–8o) shows that the SD(TAD)s at the mid-latitude location 32.5°S are relatively flat with Kp index for all λ_{track} ranges. Similar to the third row, this is likely because GWs excited by the aurora do not generally propagate to these mid-latitude locations.

We now apply the L-S linear fit and the extrapolation method (for $Kp \leq 3$) to all of the bins in the GOCE SD(TAD)s maps (see Figures 3 and 4) using the same method as depicted in Figure 4. The extrapolated SD(TAD)s at $Kp = 0$ (y-intercepts) and the linear slopes of the fits are shown in the first and second rows in Figure 9, respectively. The third row consists of southern polar view maps of the first two rows. We consider these SD(TAD) extrapolated maps (to $Kp = 0$) to be our most-quantitative and most-accurate quiet time results at GOCE altitudes.

In the first row of Figure 9 and in Figures 9g–9i, we see the remarkable result that there is a clear TAD hotspot over the Southern Andes-Antarctica Peninsula region, which is clearest and strongest for small-medium-scale λ_{track} TADs. As we go from left to right (from the small-medium-scale to large-scale λ_{track} TADs), this hotspot grows weaker as the TADs are instead concentrated in an approximately circular region over the Antarctic continent which is approximately centered on the geographic South pole (Note that this circular TAD distribution is also seen for small-medium-scale TADs, although it is somewhat weaker in amplitude). It is important to note that the circular region over the Antarctic continent is not centered on the geomagnetic South pole. Therefore, it is very unlikely that these TADs are generated by sources related to geomagnetic disturbances. For medium and large λ_{track} ranges in the first row of Figure 9 and in Figures 9g–9i, the amplitudes of the TADs are large at geographic longitudes of ~60°W and 120°–180°E and are small at geographic longitudes of ~120°W and ~60°E. However, caused by the lack of density observations at the latitudes of 85°–90°S due to the limited orbit inclination of the GOCE satellite (~96.7°), we are not confident

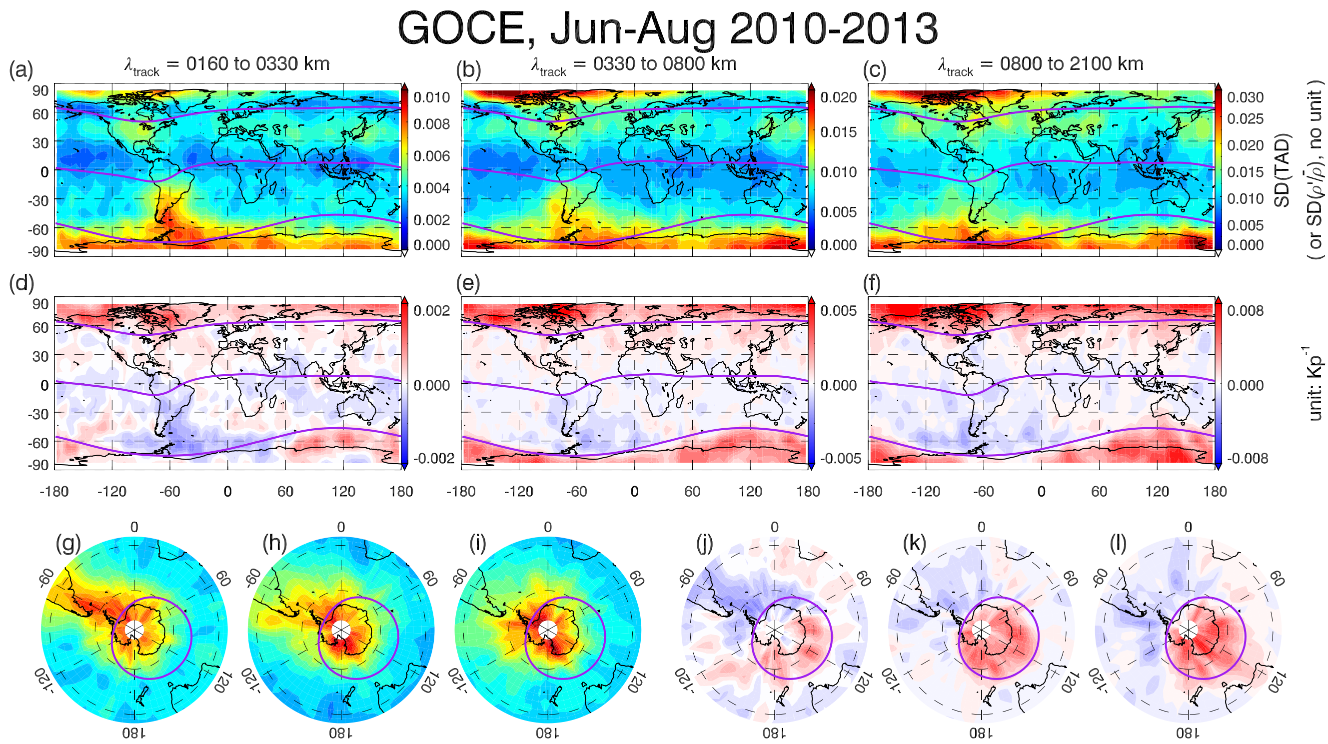

Figure 9. (a–c) The extrapolated SD(TAD) distributions at $Kp = 0$ (i.e., the Y-intercepts of the linear fits for each 5° × 5° bin) obtained from the GOCE data for traveling atmospheric disturbances with λ_{track} = 160–330 km, λ_{track} = 330–800 km, and λ_{track} = 800–2,100 km, respectively. (d–f) Slopes of the linear fits (i.e., the 1 degree term coefficient) of SD(TAD) versus Kp when $0 < Kp \leq 3$ for the same λ_{track} ranges, respectively. The third row, left to right, shows the south polar view maps for panels (a–f), respectively. The maps in the panels are smoothed with a boxcar average of 3 × 3 bins centered at each 5° × 5° map bin.

whether this indicates a possible bimodal (horizontal) distribution of TADs around the geographic South pole. Fortunately, because of the more vertical inclination of the CHAMP satellite (~87°), the before-mentioned bimodal distribution is very clear for large-scale λ_{track}TADs at the CHAMP's altitude (see Section 4.2).

We now examine the GW dispersion relation in order to confirm that the TAD hotspots in Figures 9g–9i are generated from the Southern Andes-Antarctic Peninsula region. At GOCE's altitude of $z \sim 250$ km, the GWs with maximum momentum flux (i.e., that have not yet dissipated from molecular viscosity) have vertical wavelengths of $\lambda_z \sim 100 - 200$ km (Vadas, 2007), so it is reasonable to assume $m^2 \gg \alpha^2$, where m is the vertical wavenumber defined by $m = 2\pi/\lambda_z$, α is defined by $\alpha = 1/\left(2H_\rho\right)$ and H_ρ is the density scale height. If the intrinsic wave frequency ω_{Ir} and inertial frequency f satisfy $\omega_{Ir} \gg f$, then Equation 1 in Marks and Eckermann (1995) can be simplified as

$$\frac{{\omega_{Ir}}^2}{N^2} = \cos^2\theta = \frac{{k_H}^2}{{k_H}^2 + m^2} \tag{1}$$

where N is the buoyancy frequency, $k_H = 2\pi/\lambda_H$ is the horizontal wave number, and θ is the angle between the vertical and the GW propagation. We denote ΔL and ΔZ as the horizontal and vertical distances, respectively, traveled by a GW as it propagates from the excitation source location to GOCE's location. Since $\tan\left(\theta\right) = \Delta L/\Delta Z$, then from Equation 1 we get

$$\Delta L = \Delta Z \times \tan\theta = \Delta Z \times \frac{\lambda_H}{\lambda_z}. \tag{2}$$

Therefore, if a (lower-frequency) GW is generated at an altitude of $z = 100$ km with $\lambda_z = 100$ km and $\lambda_H = 2000$ km, then when it reaches the altitude of $z = 250$ km, it has traveled horizontally by the large distance of $\Delta L = \Delta Z \times \lambda_H/\lambda_z = \left(150\text{ km}\right) \times 20 = 3000$ km. Note that 3,000 km is the distance from the tip of the Antarctic Peninsula to the South pole. On the other hand, if a (high-frequency) GW has $\lambda_H = 200$ km (and the same λ_z) instead, then it only travels horizontally $\Delta L = 300$ km in reaching GOCE altitudes.

In order to obtain a better understanding of the relationship between TADs and geomagnetic activity, we now focus on the linear slopes of the fits in Figures 9d–9f and 9j–9l. The red (blue) color indicates a positive (negative) correlation of the SD(TAD) with the *K*p index. It is evident that the TADs in the Southern Andes-Antarctic region have a weak (negative) correlation with *K*p. In Figure 7 of Hedin and Mayr (1987), the variation in the GW amplitude in the long-wavelength band has a stronger correlation with the geomagnetic index, while it is relatively constant in the short-wavelength range during the geomagnetically quiet time. In our Figures 9j–9l, similar results are found in the correlations between SD(TAD)s and *K*p. In the opposite direction of the Southern Andes, that is, at 120°E, the protruding reddish pattern for large-scale TADs (λ_{track} ~ 800–2,100 km) suggests a stronger correlation between SD(TAD)s and *K*p for larger-scale TADs.

In general, the quiet time TADs extrapolated from the GOCE data agree well with the results of the HIAMCM model study (Becker & Vadas, 2020). Comparing the results in Figures 12d–12i of Becker and Vadas (2020) to Figures 9g–9i from this study, consistent morphological traits can be observed: for the small-medium-scale TADs with λ_{track} = 160–330 km, the hotspot completely covers the Southern Andes-Antarctic region, and the strongest peak is slightly east of the Southern Andes. However, for the TADs with medium- and large-scale λ_{track}, the TADs from the Southern Andes-Antarctic region are distributed around and over the South pole at the GOCE altitudes. As mentioned previously, this is because the large-scale λ_H GWs propagate large distances horizontally in reaching GOCE altitudes. Notably, Becker and Vadas (2020) found that the amplitudes of tertiary GWs with large λ_H were significantly smaller downstream of the Southern Andes-Antarctic Peninsula at 60°W to 40°E than at 120°E; this was due to the large horizontal distances propagated by these lower-frequency GWs. However, in Figure 9i, there are larger-amplitude TADs at 60°W to 40°E, which seemingly contradicts these model results. As mentioned previously when describing Figures 4c and 6b–6c in Section 3, this is because TADs with larger-scales includes GWs with small-medium λ_H having significant zonal components to their propagation directions (since GOCE traveled mostly meridionally). These small-medium λ_H GWs do not propagate very far horizontally in reaching GOCE altitudes, and therefore "contaminate" the larger-scale SD(TAD) map at 60°W–40°E over Antarctica (near the Antarctic Peninsula).

4.2. Quiet Time TADs at CHAMP Altitudes

Analogous to the linear fit analyses we applied to the GOCE data shown in Figures 8 and 9, we now apply the same analyses to the CHAMP data. The analogous TAD results are shown in Figures 10 and 11. Similar to the GOCE results, when *K*p > 3, the SD(TAD)s increase steeply for medium and large-scale λ_{track} TADs (second and third columns in Figure 10) at the geomagnetic latitude ~65°S (Figures 10b and 10c), at the geomagnetic latitude ~60°S (Figures 10e–10f), and over Wilkes Land (Figures 10k–10l) at the CHAMP altitudes. However, in all regions, the SD(TAD)s for the small-medium-scale λ_{track} TADs (first column) are relatively flat or even decrease somewhat with increasing *K*p when 0 < *K*p ≤ 3.0.

We apply linear fits to each map bin in the SD(TAD) maps and extrapolate the results to *K*p = 0. The resulting quiet time maps are shown in Figure 11. The distribution of TAD activity from the CHAMP data for TADs with λ_{track} = 330–800 km (Figure 11b) is similar to that reported by Trinh et al. (2018). Comparing the extrapolated SD(TAD)s at *K*p = 0 at the CHAMP altitudes (the first row of Figure 11) to those at the GOCE altitudes (the first row of Figure 9), it is clear that the TAD hotspot at the CHAMP altitudes directly over the Southern Andes region is weaker for small-medium-scale λ_{track} TADs, is stronger for medium-scale λ_{track} TADs, and is much stronger for large-scale λ_{track} TADs. As mentioned previously, the fact that the amplitude of the Southern Andes hotspot due to GWs with small-medium scales is much smaller at CHAMP than at GOCE altitudes is supported by model results (Becker & Vadas, 2020), and stems from the fact that GWs with small-medium λ_H typically have smaller horizontal phase speeds and vertical wavelengths, and therefore dissipate from molecular viscosity between GOCE and CHAMP altitudes (Vadas, 2007).

The bimodal horizontal TAD distribution that we previously saw some indication of in the GOCE data (in Figure 9i) is clearly visible for medium- and large-scale λ_{track} TADs in Figures 11b and 11c and Figures 11h and 11i. One peak of this bimodal distribution occurs over and east of the Southern Andes region at 50°S–90°S and 120°W–50°E, and the other is over the Wilkes Land (which contains the geomagnetic South pole) at 60°S–90°S and 80°E–170°E. Previous studies analyzing the GOCE and CHAMP data for *K*p < 3 or *Kp* < 4 also contained this bimodal distribution (H. X. Liu et al., 2017; Park et al., 2014; Trinh

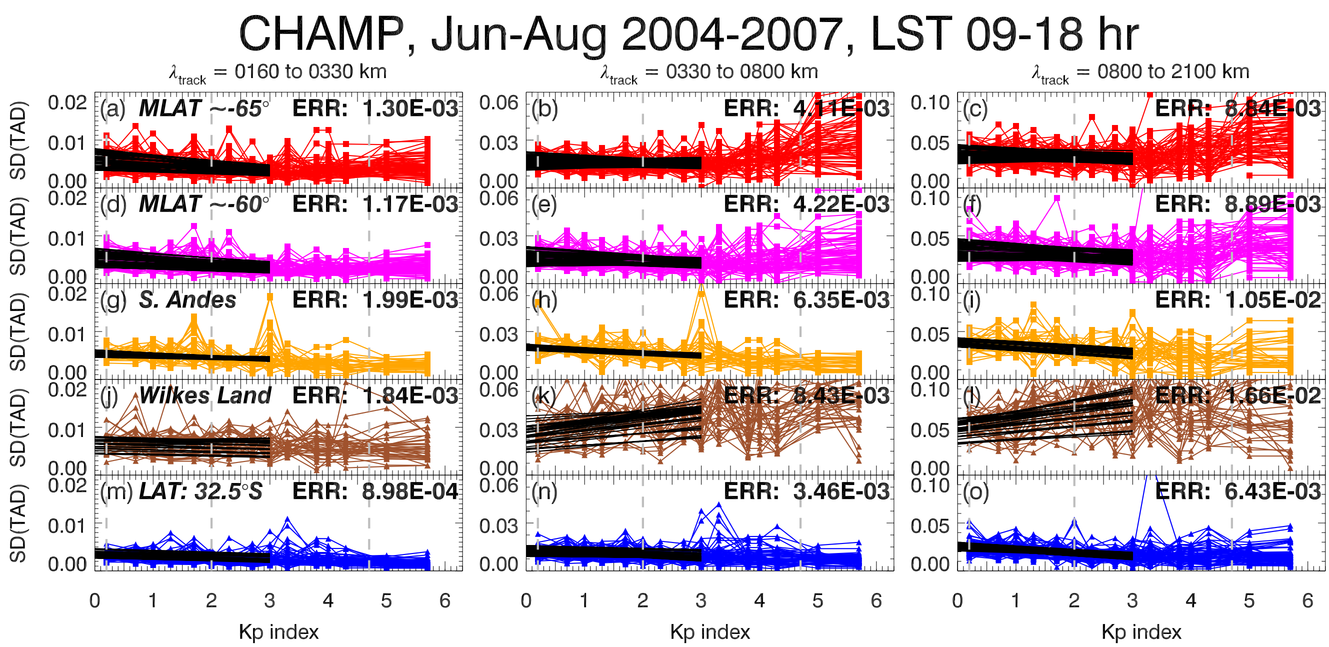

Figure 10. The same as Figure 8 but for CHAMP data during LST 9–18 h, June–August 2004–2007. The SD(TAD)s contain no smoothing here. The gray dashed vertical lines correspond to the 3 selected Kp levels in Figure 5 rows (a–c).

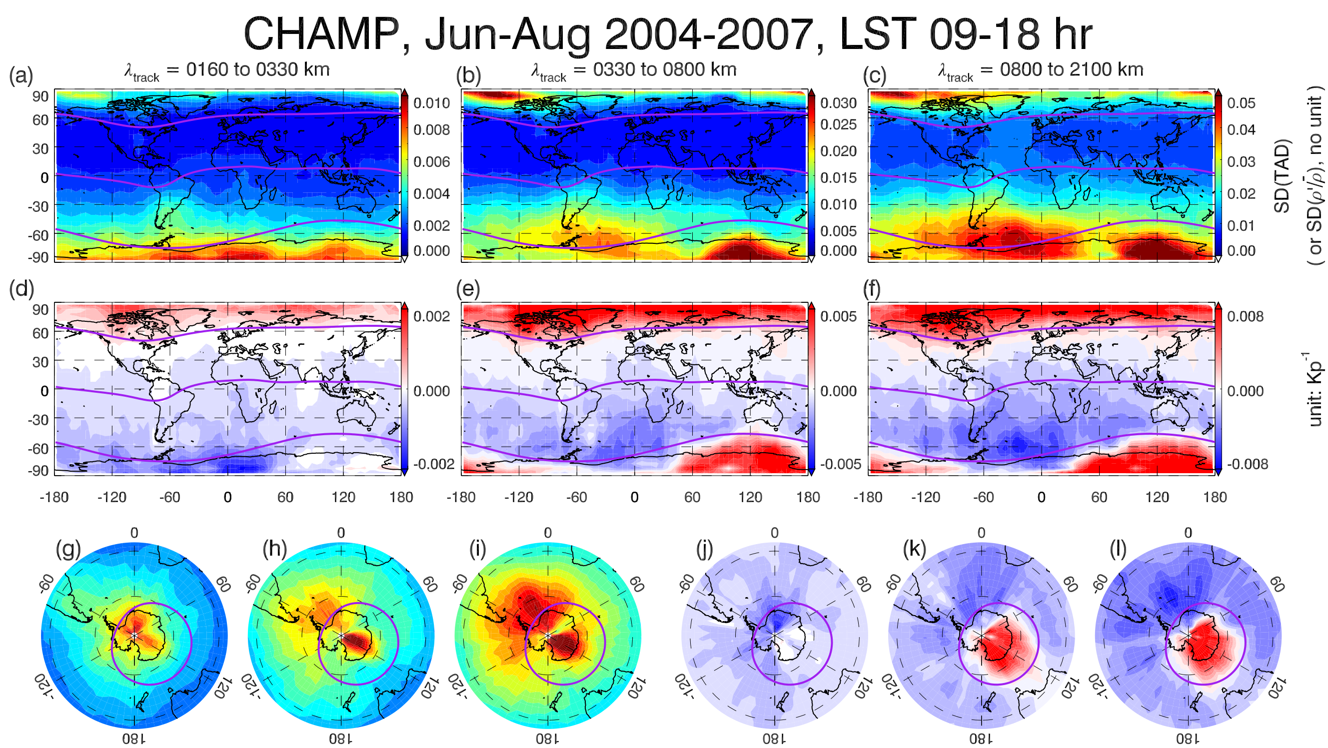

Figure 11. (a–c) The extrapolated SD(TAD) for CHAMP at $Kp = 0$ (i.e., the Y-intercepts of the linear fits for each 5° × 5° bin) for traveling atmospheric disturbances with λ_{track} = 160–330 km, λ_{track} = 330–800 km, and λ_{track} = 800–2,100 km, respectively. (d–f) Slopes of the linear fits (i.e., the 1 degree term coefficient) of SD(TAD) versus Kp when $0 < Kp \leq 3$ for the same λ_{track} ranges, respectively. The third row, left to right, shows the south polar view maps for panels (a–f), respectively. The maps in the panels are smoothed with a boxcar average of 5 × 5 bins centered at each 5° × 5° map bin.

et al., 2018). However, although their figures show this bimodal distribution, they did not quantify or eliminate the influence of geomagnetic disturbances, and generally viewed the high TAD amplitudes over Antarctica as geomagnetic induced. Using the HIAMCM, Becker and Vadas (2020) found that there is a peak in the GW temperature (or density) perturbations for GWs with large-scale λ_H at 60°E–180°E, in the vicinity of the Wilkes Land. These GWs are not created by geomagnetic activity, but are instead tertiary GWs from mountain wave breaking over the Southern Andes-Antarctic Peninsula. They are located a large distance from these orographic sources because they are lower-frequency GWs and therefore propagate large distances horizontally in reaching CHAMP altitudes. This explains the latter TAD hotspot in Figures 11h–11i. The former hotspot likely occurs because the large-scale λ_{track} GWs are "contaminated" with medium-scale λ_H GWs, which travel shorter horizontal propagation distances from their sources (see above).

It is worth noting that in Figure 11d for the small-scale λ_{track} TADs, there is almost no positive correlation between SD(TAD)s and Kp in the Southern Hemisphere, including in the South polar region. This is caused by a substantial increase in the background density $\overline{\rho}$ as Kp increases. It is also evident that during quiet time, the initial source of most TADs having small λ_{track} is non-geomagnetic related, but is ultimately from orographic GWs.

5. Conclusions

In this study, we calculate the thermospheric TAD distributions during the quiet time in austral winter from multi-year density observations from GOCE and CHAMP. We extract the TADs from the data using a filtering method that is more precise than routine methods such as the sliding window average, then group the results into three λ_{track} ranges and multiple Kp levels. We utilize a new method to rigorously extrapolate our results to $K\text{p} = 0$ in order to obtain more-precise quiet time TAD distributions which better-exclude the influence from geomagnetic disturbances. We also evaluate the correlation of the TAD distributions with the Kp index in order to better-understand the sources of the TADs at high latitudes over Antarctica in the Southern Hemisphere.

We first used a quasi-box shaped Butterworth band-pass filter to extract the waves from in-situ density observations. This process produces fine structure TAD distributions for different λ_{track} and Kp ranges. We find that the TAD amplitudes, SD($\rho'/\overline{\rho}$), both increase with the Kp index or are relatively flat/slightly decrease with the Kp index, depending on the location. In particular, the amplitudes of the medium and large-scale TADs increase with Kp in the region around the geomagnetic pole (Wilkes Land) at the GOCE and CHAMP altitudes and at geomagnetic latitude 65°S at the GOCE altitude; this is due to the fact that increasing geomagnetic activity leads to the excitation of GWs that propagate to GOCE and CHAMP altitudes, thereby causing the amplitude of $\rho'/\overline{\rho}$ to increase. Whereas at both GOCE and CHAMP altitudes, the amplitude is flat or slightly decreases in the Southern Andes-Antarctic region, at the geomagnetic latitude 60°S, and at 32.5°S. Such a decrease may seem surprising, and occurs as follows. The Kp index increases when energy from the magnetosphere is inputted into the thermosphere (in the form of energetic particles), which causes the background thermospheric temperature and density $\overline{\rho}$ (at a given altitude) to increase, thereby causing the thermosphere to expand. This causes the denominator of $\rho'/\overline{\rho}$ to increase. Near the geomagnetic pole, ρ' can increase by much more than the increase in $\overline{\rho}$ because of the creation of TADs from this geomagnetic activity. However, away from the geomagnetic pole, ρ' stays approximately the same (or only increases a small amount) because most of the TADs excited by this activity cannot propagate to this location. At these latter locations, the end result is that $\rho'/\overline{\rho}$ decreases for increasing Kp. Since most of the Antarctic continent is located at the intersection of these two regions, it is useful to compute the dependence of SD(TAD) on Kp to determine the TAD sources at high geomagnetic latitudes, as we have done here. Note that in previously published works, it was difficult to determine the sources of the TADs at these high latitude regions from GOCE and CHAMP data via only including all data with $K\text{p} \leq 3$ (which has been conventionally called the "quiet time"). This is because $K\text{p} \leq 3$ contains TADs created from geomagnetic disturbances, high energy particle precipitation, etc. Such TADs appear to be most prevalent at geomagnetic latitudes greater than 60°S. At nearly all other locations, however, even at high geographic latitudes close to the Antarctic Peninsula, we find that the $K\text{p} \leq 3$ TADs are nearly all true quiet time TADs. This is especially true over the Southern Andes-Antarctic Peninsula and at geomagnetic latitudes less than 60°S. Thus, we find that the "quiet time" $K\text{p} \leq 3$ hotspot TADs over the Southern Andes-Antarctic Peninsula originally originate from below (tropospheric GWs, e.g., MWs) via multi-step vertical coupling. Therefore, the Kp ≤ 3 "quiet time" criterion still holds at most locations, but it should be used cautiously case by case, because it does not strictly indicate that it is "geomagnetic disturbance free."

We then minimized the influences associated with the Kp index by extrapolating the TAD distributions to Kp = 0. We found that the TADs with different along-track wavelengths λ_{track} have spatially different hotspot distributions in the Austral winter at the GOCE altitudes. For TADs with small-medium wavelengths, the hotspots not only occur over the Southern Andes-Antarctic Peninsula region (tropospheric orographic sources), but also stretch downstream (east) somewhat and to geographic higher latitudes around the South pole region over the Antarctic continent. The close proximity to the underlying orography can be explained by the fact that small-medium-scale (tertiary) GWs have high frequencies, and therefore do not propagate very far horizontally as they propagate upward to GOCE altitudes. In contrast, for TADs with large-scale along-track wavelengths, the TAD hotspot is located over the Antarctic continent region. These are mostly the large λ_H tertiary GWs from mountain wave breaking which have smaller frequencies and therefore propagate larger distances horizontally when they reach GOCE altitudes. This is why the hotspot is over Antarctica, relatively far from the Southern Andes. However, these TADs also include small and medium λ_H GWs (having significant zonal propagation components) that propagate closer to the zenith. The medium-scale TAD distribution is a combination of the small-medium and large-scale TAD distributions. The morphology of the TAD hotspot over the Southern Andes-Antarctic Peninsula region is in agreement with former observations. However, our discovery that there are actually two distinct orographic hotspots (over Southern Andes-Antarctic Peninsula and Antarctic continent, depending on λ_H) is a new observational result, and is in agreement with model simulations (Becker & Vadas, 2020).

Finally, we found that at the CHAMP altitudes and during the day time (LST 9–18) during 2004–2007, the hotspot of the small-medium-scale TADs over the Southern Andes-Antarctic Peninsula is very weak. This occurs because these high-frequency GWs have smaller horizontal phase speeds and vertical wavelengths, and therefore dissipate from molecular viscosity between GOCE and CHAMP altitudes. However, the distributions for the medium- and large-scale TADs make up a bimodal horizontal distribution over the southern polar region. One peak of the bimodal distribution is located slightly east to the Southern Andes-Antarctic Peninsula, while the other is smaller and is more concentrated over the Wilkes Land. This bimodal distribution was recently modeled by Becker and Vadas (2020), and occurs because of the following. The tertiary GWs from mountain wave breaking are created downstream (east) of the Southern Andes-Antarctic Peninsula, near where the polar night jet is maximum (~60°S) (Vadas & Becker, 2019). Those tertiary GWs with large horizontal wavelengths propagate large horizontal distances, around and over the pole, while propagating to CHAMP altitudes. This creates the large TAD hotspot over Antarctica at longitudes opposite to the Antarctic Peninsula, even though there is very weak geomagnetic activity. However, because the large-scale λ_{track} TADs also contain GWs with medium λ_H, there is also the TAD hotspot closer to the Southern Andes-Antarctic Peninsula for these large-scale λ_{track} TADs.

We remind the readers that for this current research, we study the TADs as a function of along-track horizontal wavelength λ_{track} instead of λ_H. In the future, we will use the polarization and dispersion relationship of GWs, combined with the background atmosphere conditions, to derive the more-complete, intrinsic properties of GWs (including propagation directions) observed by the GOCE and CHAMP satellites (e.g., Vadas et al., 2019).

Appendix A: Extraction of TADs for Specific λ_{track} Range

The extraction of waves from in-situ density data such as GOCE and CHAMP have traditionally been carried out by applying a sliding window average such as a low-pass filter. For example, Bruinsma and Forbes (2007) extracted waves along the CHAMP track from 1,300 to 5,600 km by applying a running average window twice successively with 2 widths, and Forbes et al. (2016) calculated the RMS (root mean square) of the density and wind residuals by removing the running average along the GOCE orbit. Similar to the running mean, Park et al. (2014) and Trinh et al. (2018) used the Savitzky-Golay low-pass filter on the CHAMP data to yield a smoothed background density. However, to prevent waves outside of the intended λ_{track} range from "leaking" into the residuals (i.e., ρ'), we used the quasi-box shaped Butterworth band-pass filter (assembled with 2 high-order Butterworth filters) to yield the density variability in the λ_{track} range of interest.

Unlike simpler methods like the running average, the quasi-box shaped filter should be applied to a track of a finite length. For computational considerations, we divide the GOCE and CHAMP data sets into segments no longer than one full-circle orbit. Figure A1 shows the data processing steps: the GOCE data is first processed in the time-latitude sequence, and then filtered by the Butterworth filters to get the TAD information in different λ_{track} ranges. In Figures A1a and A1b, the GOCE v1.5 density data in 2010 June is divided by the Ascending-Descending (AD) and Descending-Ascending (DA) modes, respectively. In Figures A1c and A1d, the GOCE density data in July 2010 is divided in the same way. The term "AD mode" denotes a track starting with a satellite in an ascending mode to its position in the following descending mode, and vice versa for the DA mode. At the same time, the satellite observes continuously, generating one data point per 10 s without any missing data in a length no longer than one full-circle orbit. A missing data point within an AD track will cause a break in the temporal continuity of the density information, making the spectral analysis more difficult. Therefore, a missing data point will end the track before the following descending track. For example, in Figures A1c and A1d, we find that the missing data points in the GOCE data set in July 2010 at Time = ~16.05 h (14:00 GPS + 7370–7410 s, ~55°N) and ~17.56 h (14:00 GPS + 12800–12830 s, ~58°N) cause breaks in the tracks #2 & #4 in Figure A1c and breaks in tracks #2 & #4 in Figure A1d, generating two short DA tracks #3 & #5. The gray bolded parts show the terminations of each track, and the band-pass filtered results of the terminations can introduce fictitious errors due to the

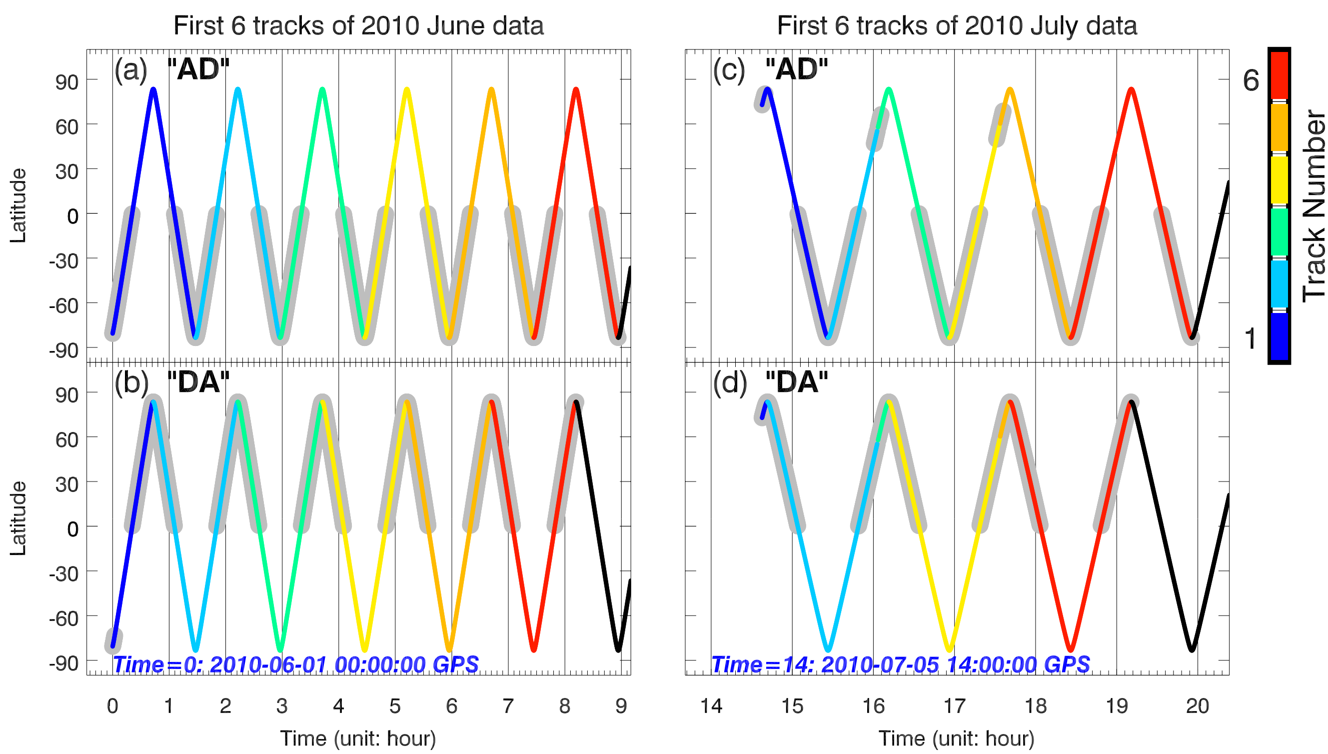

Figure A1. The four panels show how the GOCE orbit (latitude vs. time) is divided into tracks and is allocated with specific track numbers. Only the first 6 tracks in each panel are shown with the corresponding colors in the color-bar. (a and b) in the left column show that the June 2010 data points are divided into "AD" and "DA" methods, respectively. (c and d) in the right column show the same as the left column but for the July 2010 data.

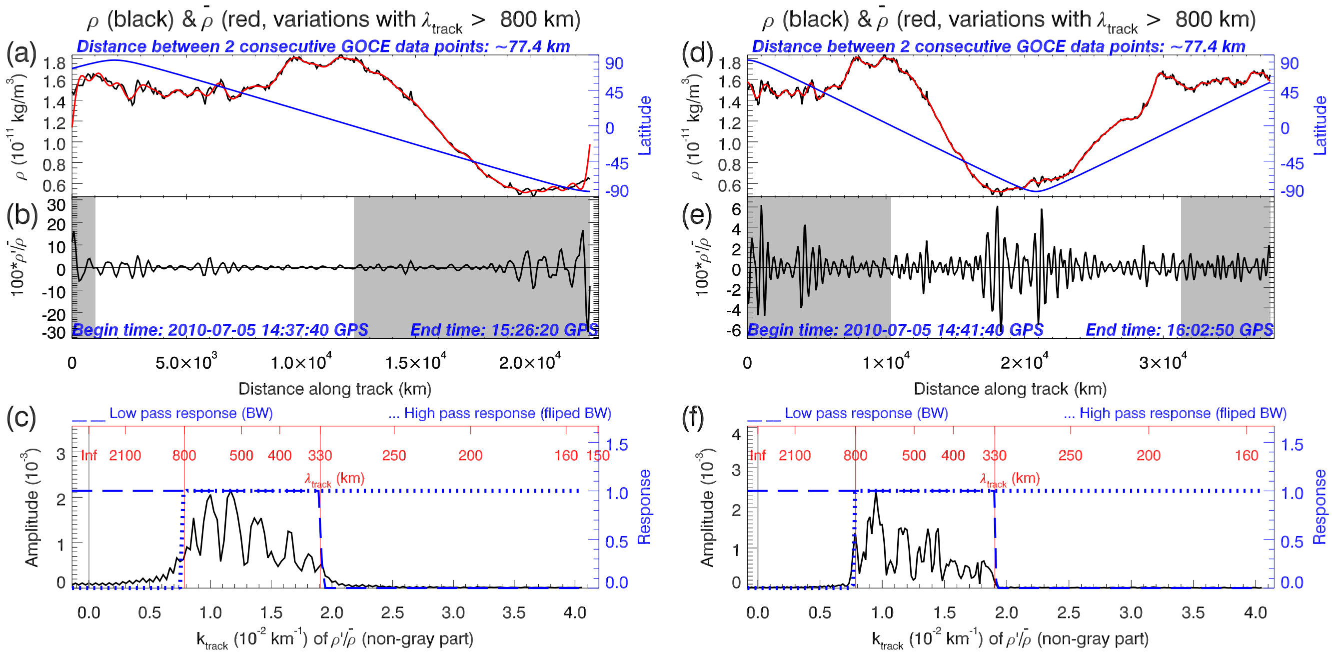

Figure A2. Examples of the application of the quasi-box shaped Butterworth band-pass filter to (a–c) a part-circle track and (d–f) a nearly full-circle track. (a) The absolute density measurements ρ (black) of track #1 in Figure A1c, a part-circle track, the background density $\bar{\rho}$ that consists of waves with λ_{track}> 800 km (red), and the corresponding latitude for each data point (blue). (b) The black curve shows the traveling atmospheric disturbance (TAD) $\rho'/\bar{\rho}$ (in percent), where ρ' is the low-pass part of $\left(\rho - \bar{\rho}\right)$ at λ_{track}>300 km. (c) The FFT spectrum of the TAD data of the non-gray part in (b), which shows that almost all of the wave components fall into the λ_{track} range of 330–800 km. The Butterworth band-pass filtered TAD in the gray shaded part at the terminations of a track often has a very high magnitude and should be removed before merging global TAD distribution; (d–f) The same as (a–c) but for the input track #2 in Figure A1d.

Gibbs phenomenon. They are discussed in Figure A2 and eventually discarded for analysis. Also, the bolded shaded part in Figure A1 is similar to the gray shaded part in Figure A2.

Figure A2 shows the application of the quasi-box shaped Butterworth band-pass filter on two specific GOCE orbit segments to derive the TADs in the medium wavelength range (λ_{track} = 330–800 km). Figure A2a shows the absolute density (black) and latitude (blue) along the AD track #1 in 2010 July, which is also denoted by the blue track in Figure A1c. Figure A2d is same as Figure A2a but for the DA track #2 in July 2010 (the azure track in Figure A1d). Let's take the case in the left column of Figure A2 for example. First, we use a low-pass Butterworth filter that cuts off at λ_{track} = 800 km to obtain the "background" density $\bar{\rho}$, which is plotted in red in Figure A2a. Then the fluctuation is obtained from $\left(\rho - \bar{\rho}\right)$ part. By applying a low-pass Butterworth filter with a cutoff frequency of λ_{track} = 330 km, the sine wave components ρ' in λ_{track} = 330–800 km is obtained from the fluctuation. The reconstructed variability is shown as $\left(\rho'/\bar{\rho}\right)$ in Figure A2b, and the response curves of the two filters are shown as the blue dotted and blue dashed lines in Figure A2c. The black curve in Figure A2c is the FFT spectra of $\rho'/\bar{\rho}$ in the non-gray shaded part in Figure A2b; we see that $\rho'/\bar{\rho}$ mostly falls quite well in the range λ_{track} = 330–800 km. The processes behind the right column of Figure A2 are same as those in the left column but for the azure track.

Our quasi-box shaped band-pass filter extracts the information in the frequency domain much more effectively than routine methods such as the sliding window average. The results from the quasi-box band pass filter, the sliding average smooth method, and the Savitzky–Golay filter method are shown in the right column of Figure A2, the left column of Figure A3 and the right column of Figure A3, respectively. It is obvious that the latter two methods both result in considerable residues outside the λ_{track} range of interest, which is caused by the soft cutoffs at the boundaries of the λ_{track} range for both response curves.

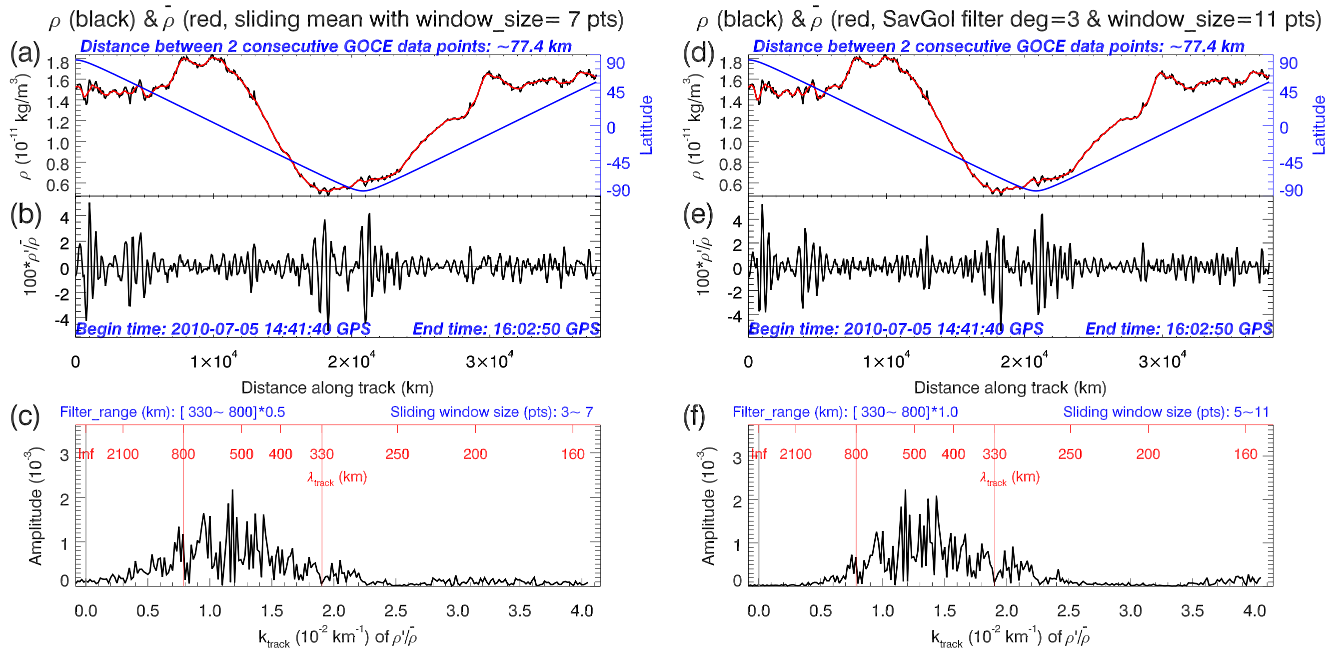

Figure A3. (a–c): the same as in Figures A2d–A2f with the same λ_{track} range that is, 330–800 km, except that $\bar{\rho}$ (red curve) is smoothed from ρ by a sliding mean with a window size equals to 3 data points (∼155 km); (d–f): the same as in (a–c) except that $\bar{\rho}$ (red curve) is smoothed by a Savitzky–Golay filter with the sliding-window size for the filter range of interest.

Data Availability Statement

*K*p data is available here: https://www.ngdc.noaa.gov/stp/GEOMAG/kp_ap.html; Time Series Solar Radio Flux at 10.7cm data is available here: http://lasp.colorado.edu/lisird/data/noaa_radio_flux/; GOCE v1.5 data are downloaded here: https://earth.esa.int/web/guest/missions/esa-operational-missions/goce/goce-thermospheric-data; The CHAMP data access is: http://thermosphere.tudelft.nl/.

Acknowledgments

S. Xu and S.L. Vadas were supported by NSF Grant AGS-1832988 and by NASA grants 80NSSC19K0836 and 80NSSC20K0628. J. Yue was supported by NSF grants AGS-1651394, AGS-1834222 and by NASA AIM and 80NSSC20K0628. S. Xu would like to thank Dr. James M. Russell III, Dr. Christian Siemes, Dr. Huixin Liu, Dr. Wenbin Wang and Simin Zhang for helpful discussions.

References

Alexander, M. J., Holton, J. R., & Durran, D. R. (1995). The gravity-wave response above deep convection in a squall line simulation. *Journal of the Atmospheric Sciences*, *52*(12), 2212–2226. https://doi.org/10.1175/1520-0469(1995)052<2212:tgwrad>2.0.co;2

Azeem, I., Vadas, S. L., Crowley, G., & Makela, J. J. (2017). Traveling ionospheric disturbances over the United States induced by gravity waves from the 2011 Tohoku tsunami and comparison with gravity wave dissipative theory. *Journal of Geophysical Research: Space Physics*, *122*(3), 3430–3447. https://doi.org/10.1002/2016ja023659

Azeem, I., Yue, J., Hoffmann, L., Miller, S. D., Straka, W. C., & Crowley, G. (2015). Multisensor profiling of a concentric gravity wave event propagating from the troposphere to the ionosphere. *Geophysical Research Letters*, *42*(19), 7874–7880. https://doi.org/10.1002/2015gl065903

Becker, E., & Vadas, S. L. (2018). Secondary gravity waves in the winter mesosphere: Results from a high-resolution global circulation model. *Journal of Geophysical Research: Atmospheres*, *123*(5), 2605–2627. https://doi.org/10.1002/2017jd027460

Becker, E., & Vadas, S. L. (2020). Explicit global simulation of gravity waves in the thermosphere. *Journal of Geophysical Research: Space Physics*, *125*, e2020JA028034. https://doi.org/10.1029/2020ja028034

Bruinsma, S. L., & Forbes, J. M. (2007). Global observation of traveling atmospheric disturbances (TADs) in the thermosphere. *Geophysical Research Letters*, *34*(14), L14103. https://doi.org/10.1029/2007gl030243

Bruinsma, S. L., & Forbes, J. M. (2008). *Properties of traveling atmospheric disturbances (TADs) inferred from CHAMP and GRACE accelerometer observations* (Vol. 2008, pp. SA21B–1541). AGUFM.

Choi, H. J., Chun, H. Y., & Song, I. S. (2007). Characteristics and momentum flux spectrum of convectively forced internal gravity waves in ensemble numerical simulations. *Journal of the Atmospheric Sciences*, *64*(10), 3723–3734. https://doi.org/10.1175/jas4037.1

Chun, H. Y., & Kim, Y. H. (2008). Secondary waves generated by breaking of convective gravity waves in the mesosphere and their influence in the wave momentum flux. *Journal of Geophysical Research*, *113*(D23), D23107. https://doi.org/10.1029/2008jd009792

Crowley, G., Jones, T. B., & Dudeney, J. R. (1987). Comparison of short-period tid morphologies in Antarctica during geomagnetically quiet and active intervals. *Journal of Atmospheric and Terrestrial Physics*, *49*(11–12), 1155–1162. https://doi.org/10.1016/0021-9169(87)90098-5

Dewan, E. M., Picard, R. H., O'Neil, R. R., Gardiner, H. A., Gibson, J., Mill, J. D., et al. (1998). MSX satellite observations of thunderstorm-generated gravity waves in mid-wave infrared images of the upper stratosphere. *Geophysical Research Letters*, *25*(7), 939–942. https://doi.org/10.1029/98gl00640

Djuth, F. T., Sulzer, M. P., Elder, J. H., & Wickwar, V. B. (1997). High-resolution studies of atmosphere-ionosphere coupling at Arecibo Observatory, Puerto Rico. *Radio Science*, *32*(6), 2321–2344. https://doi.org/10.1029/97rs02797

Djuth, F. T., Sulzer, M. P., Gonzales, S. A., Mathews, J. D., Elder, J. H., & Walterscheid, R. L. (2004). A continuum of gravity waves in the Arecibo thermosphere? *Geophysical Research Letters*, *31*(16), L16801. https://doi.org/10.1029/2003gl019376

Doornbos, E. (2016). *ESA AO/1-6367/10/NL/AF "GOCE+ Theme 3: Air density and wind retrieval using GOCE data" Data Set User Manual for data set version 1.5*. Data Set User Manual. Retrieved from https://earth.esa.int/documents/10174/679909/GOCEPlus_Theme_3_Dataset_User_Manual

Doornbos, E., Bruinsma, S., Fritsche, B., Visser, P., Van Den IJssel, J., Encarnacao, J. T., & Kern, M. (2013). *Air density and wind retrieval using GOCE data*. Paper presented at the ESA Living Planet Symposium.

Doornbos, E., Forster, M., Fritsche, B., van Helleputte, T., van den IJssel, J., Koppenwallner, G., et al. (2009). *ESTEC contract 21022/07/NL/HE air density models derived from multi-satellite drag observations—Final report* (Vol. 1, pp. 7–39). DEOS/Delft University of Technology Scientific TR.

Feldstein, Y. I., & Galperin, Y. I. (1985). The auroral luminosity structure in the high-latitude upper atmosphere: Its dynamics and relationship to the large-scale structure of the Earth's magnetosphere. *Reviews of Geophysics*, *23*(3), 217–275. https://doi.org/10.1029/rg023i003p00217

Forbes, J. M. (1995). Tidal and planetary waves. The upper mesosphere and lower thermosphere: A review of experiment and theory (Vol. 87, pp. 67–87). Geophys. Monogr. Ser.

Forbes, J. M., Bruinsma, S. L., Doornbos, E., & Zhang, X. L. (2016). Gravity wave-induced variability of the middle thermosphere. *Journal of Geophysical Research: Space Physics*, *121*(7), 6914–6923. https://doi.org/10.1002/2016ja022923

Fritts, D. C., & Alexander, M. J. (2003). Gravity wave dynamics and effects in the middle atmosphere. *Reviews of Geophysics*, *41*(1), 1003. https://doi.org/10.1029/2001rg000106

Georges, T. M. (1968). Hf doppler studies of traveling ionospheric disturbances. *Journal of Atmospheric and Terrestrial Physics*, *30*(5), 735, 746. https://doi.org/10.1016/s0021-9169(68)80029-7

Heale, C. J., Bossert, K., Vadas, S. L., Hoffmann, L., Dornbrack, A., Stober, G., et al. (2020). Secondary gravity waves generated by breaking mountain waves over Europe. *Journal of Geophysical Research: Atmospheres*, *125*(5), e2019JD031662. https://doi.org/10.1029/2019jd031662

Heale, C. J., Lund, T. S., & Fritts, D. C. (2020). Convectively generated gravity waves during solstice and equinox conditions. *Journal of Geophysical Research: Atmospheres*, *125*(9), e2019JD031582. https://doi.org/10.1029/2019jd031582

Heale, C. J., Snively, J. B., Bhatt, A. N., Hoffmann, L., Stephan, C. C., & Kendall, E. A. (2019). Multilayer observations and modeling of thunderstorm-generated gravity waves over the midwestern United States. *Geophysical Research Letters*, *46*(23), 14164–14174. https://doi.org/10.1029/2019gl085934

Hedin, A. E., & Mayr, H. G. (1987). Characteristics of wavelike fluctuations in Dynamics Explorer neutral composition data. *Journal of Geophysical Research*, *92*(A10), 11159–11172. https://doi.org/10.1029/ja092ia10p11159

Hickey, M. P., & Cole, K. D. (1988). A numerical-model for gravity-wave dissipation in the thermosphere. *Journal of Atmospheric and Terrestrial Physics*, *50*(8), 689–697. https://doi.org/10.1016/0021-9169(88)90032-3

Hines, C. O. (1964). *Atmospheric gravity waves-a new toy for the wave theorist*.

Hocke, K., & Schlegel, K. (1996). A review of atmospheric gravity waves and travelling ionospheric disturbances: 1982-1995. *Annales Geophysicae-Atmospheres Hydrospheres and Space Sciences*, *14*(9), 917–940. https://doi.org/10.1007/s00585-996-0917-6

Hocke, K., Schlegel, K., & Kirchengast, G. (1996). Phases and amplitudes of TIDs in the high latitude F-region observed by EISCAT. *Journal of Atmospheric and Terrestrial Physics*, *58*(1–4), 245–255. https://doi.org/10.1016/0021-9169(95)00033-x

Hoffmann, L., & Alexander, M. J. (2010). Occurrence frequency of convective gravity waves during the North American thunderstorm season. *Journal of Geophysical Research*, *115*(D20), D20111. https://doi.org/10.1029/2010jd014401

Hoffmann, L., Xue, X., & Alexander, M. J. (2013). A global view of stratospheric gravity wave hotspots located with atmospheric infrared sounder observations. *Journal of Geophysical Research: Atmospheres*, *118*(2), 416–434. https://doi.org/10.1029/2012jd018658

Holton, J. R., & Alexander, M. J. (1999). Gravity waves in the mesosphere generated by tropospheric convention. *Tellus Series A-Dynamic Meteorology and Oceanography*, *51*(1), 45–58. https://doi.org/10.3402/tellusa.v51i1.12305

Innis, J. L., & Conde, M. (2002). Characterization of acoustic-gravity waves in the upper thermosphere using Dynamics Explorer 2 Wind and Temperature Spectrometer (WATS) and Neutral Atmosphere Composition Spectrometer (NACS) data. *Journal of Geophysical Research*, *107*(A12), 1418. https://doi.org/10.1029/2002ja009370

Lane, T. P., Sharman, R. D., Clark, T. L., & Hsu, H. M. (2003). An investigation of turbulence generation mechanisms above deep convection. *Journal of the Atmospheric Sciences*, *60*(10), 1297–1321. https://doi.org/10.1175/1520-0469(2003)60<1297:aiotgm>2.0.co;2

Lindzen, R. S. (1981). Turbulence and stress owing to gravity-wave and tidal breakdown. *Journal of Geophysical Research*, *86*(10), 9707–9714. https://doi.org/10.1029/jc086ic10p09707

Liu, H. X., Pedatella, N., & Hocke, K. (2017). Medium- scale gravity wave activity in the bottomside F region in tropical regions. *Geophysical Research Letters*, *44*(14), 7099–7105. https://doi.org/10.1002/2017gl073855

Liu, X., Xu, J. Y., Yue, J., Liu, H. L., & Yuan, W. (2014). Large winds and wind shears caused by the nonlinear interactions between gravity waves and tidal backgrounds in the mesosphere and lower thermosphere. *Journal of Geophysical Research: Space Physics*, *119*(9), 7698–7708. https://doi.org/10.1002/2014ja020221

Marks, C. J., & Eckermann, S. D. (1995). A three-dimensional nonhydrostatic ray-tracing model for gravity waves: Formulation and preliminary results for the middle atmosphere. *Journal of the Atmospheric Sciences*, *52*(11), 1959–1984. https://doi.org/10.1175/1520-0469(1995)052<1959:atdnrt>2.0.co;2

Mayr, H. G., Harris, I., Herrero, F. A., Spencer, N. W., Varosi, F., & Pesnell, W. D. (1990). Thermospheric gravity-waves - Observations and interpretation using the Transfer-Function Model (Tfm). *Space Science Reviews*, *54*(3–4), 297–375. https://doi.org/10.1007/bf00177800

Nicolls, M. J., Vadas, S. L., Aponte, N., & Sulzer, M. P. (2014). Horizontal parameters of daytime thermospheric gravity waves and E region neutral winds over Puerto Rico. *Journal of Geophysical Research: Space Physics*, *119*(1), 575–600. https://doi.org/10.1002/2013ja018988

Ogawa, T., Igarashi, K., Aikyo, K., & Maeno, H. (1987). Nnss satellite-observations of medium-scale traveling ionospheric disturbances at southern high-latitudes. *Journal of Geomagnetism and Geoelectricity*, *39*(12), 709–721. https://doi.org/10.5636/jgg.39.709

Oliver, W. L., Otsuka, Y., Sato, M., Takami, T., & Fukao, S. (1997). A climatology of F region gravity wave propagation over the middle and upper atmosphere radar. *Journal of Geophysical Research*, *102*(A7), 14499–14512. https://doi.org/10.1029/97ja00491

Park, J., Lühr, H., Lee, C., Kim, Y. H., Jee, G., & Kim, J. H. (2014). A climatology of medium-scale gravity wave activity in the midlatitude/low-latitude daytime upper thermosphere as observed by CHAMP. *Journal of Geophysical Research: Space Physics*, *119*(3), 2187–2196. https://doi.org/10.1002/2013ja019705

Pitteway, M., & Hines, C. (1963). The viscous damping of atmospheric gravity waves. *Canadian Journal of Physics*, *41*(12), 1935–1948. https://doi.org/10.1139/p63-194

Richmond, A. (1978). Gravity wave generation, propagation, and dissipation in the thermosphere. *Journal of Geophysical Research*, *83*(A9), 4131–4145. https://doi.org/10.1029/ja083ia09p04131

Richmond, A., & Roble, R. (1979). Dynamic effects of aurora-generated gravity waves on the mid-latitude ionosphere. *Journal of Atmospheric and Terrestrial Physics*, *41*(7–8), 841–852. https://doi.org/10.1016/0021-9169(79)90127-2

Satomura, T., & Sato, K. (1999). Secondary generation of gravity waves associated with the breaking of mountain waves. *Journal of the Atmospheric Sciences*, *56*(22), 3847–3858. https://doi.org/10.1175/1520-0469(1999)056<3847:sgogwa>2.0.co;2

Schunk, R., & Nagy, A. (2009). *Ionospheres: Physics, plasma physics, and chemistry*. Cambridge university press.

Sentman, D. D., Wescott, E. M., Picard, R. H., Winick, J. R., Stenbaek-Nielsen, H. C., Dewan, E. M., et al. (2003). Simultaneous observations of mesospheric gravity waves and sprites generated by a midwestern thunderstorm. *Journal of Atmospheric and Solar-Terrestrial Physics*, *65*(5), 537–550. https://doi.org/10.1016/s1364-6826(02)00328-0

Snively, J. B. (2013). Mesospheric hydroxyl airglow signatures of acoustic and gravity waves generated by transient tropospheric forcing. *Geophysical Research Letters*, *40*(17), 4533–4537. https://doi.org/10.1002/grl.50886

Taylor, M. J., & Hapgood, M. A. (1988). Identification of a thunderstorm as a source of short period gravity waves in the upper atmospheric nightglow emissions. *Planetary and Space Science*, *36*(10), 975–985. https://doi.org/10.1016/0032-0633(88)90035-9

Touboul, P., Foulon, B., Christophe, B., & Marque, J. (2012). CHAMP, GRACE, GOCE instruments and beyond. In *Geodesy for planet Earth* (pp. 215–221). Springer. https://doi.org/10.1007/978-3-642-20338-1_26

Trinh, Q. T., Ern, M., Doornbos, E., Preusse, P., & Riese, M. (2018). Satellite observations of middle atmosphere-thermosphere vertical coupling by gravity waves. *Annales Geophysicae*, *36*(2), 425–444. https://doi.org/10.5194/angeo-36-425-2018

Vadas, S. L. (2007). Horizontal and vertical propagation and dissipation of gravity waves in the thermosphere from lower atmospheric and thermospheric sources. *Journal of Geophysical Research*, *112*(A6), A06305. https://doi.org/10.1029/2006ja011845

Vadas, S. L. (2013). Compressible f-plane solutions to body forces, heatings, and coolings, and application to the primary and secondary gravity waves generated by a deep convective plume. *Journal of Geophysical Research: Space Physics*, *118*(5), 2377–2397. https://doi.org/10.1002/jgra.50163

Vadas, S. L., & Azeem, S. I. (2020). Concentric secondary gravity waves in the thermosphere and ionosphere over the continental United States on 25-26 March 2015 from deep convection. *Journal of Geophysical Research: Space Physics*, *126*, e2020JA028275. https://doi.org/10.1029/2020JA028275

Vadas, S. L., & Becker, E. (2018). Numerical modeling of the excitation, propagation, and dissipation of primary and secondary gravity waves during Wintertime at McMurdo Station in the Antarctic. *Journal of Geophysical Research: Atmospheres*, *123*(17), 9326–9369. https://doi.org/10.1029/2017jd027974

Vadas, S. L., & Becker, E. (2019). Numerical modeling of the generation of tertiary gravity waves in the Mesosphere and Thermosphere during strong mountain wave events over the Southern Andes. *Journal of Geophysical Research: Space Physics*, *124*(9), 7687–7718. https://doi.org/10.1029/2019ja026694

Vadas, S. L., & Crowley, G. (2010). Sources of the traveling ionospheric disturbances observed by the ionospheric TIDDBIT sounder near Wallops Island on 30 October 2007. *Journal of Geophysical Research*, *115*(A7), A07324. https://doi.org/10.1029/2009ja015053

Vadas, S. L., Fritts, D. C., & Alexander, M. J. (2003). Mechanism for the generation of secondary waves in wave breaking regions. *Journal of the Atmospheric Sciences*, *60*(1), 194–214. https://doi.org/10.1175/1520-0469(2003)060<0194:mftgos>2.0.co;2

Vadas, S. L., & Liu, H. L. (2009). Generation of large-scale gravity waves and neutral winds in the thermosphere from the dissipation of convectively generated gravity waves. *Journal of Geophysical Research*, *114*(A10), A10310. https://doi.org/10.1029/2009ja014108

Vadas, S. L., & Liu, H. L. (2013). Numerical modeling of the large-scale neutral and plasma responses to the body forces created by the dissipation of gravity waves from 6 h of deep convection in Brazil. *Journal of Geophysical Research: Space Physics*, *118*(5), 2593–2617. https://doi.org/10.1002/jgra.50249

Vadas, S. L., Liu, H. L., & Lieberman, R. S. (2014). Numerical modeling of the global changes to the thermosphere and ionosphere from the dissipation of gravity waves from deep convection. *Journal of Geophysical Research: Space Physics*, *119*(9), 7762–7793. https://doi.org/10.1002/2014ja020280

Vadas, S. L., & Nicolls, M. J. (2009). Temporal evolution of neutral, thermospheric winds and plasma response using PFISR measurements of gravity waves. *Journal of Atmospheric and Solar-Terrestrial Physics*, *71*(6–7), 744–770. https://doi.org/10.1016/j.jastp.2009.01.011

Vadas, S. L., & Nicolls, M. J. (2012). The phases and amplitudes of gravity waves propagating and dissipating in the thermosphere: Theory. *Journal of Geophysical Research*, *117*(A5), A05322. https://doi.org/10.1029/2011ja017426

Vadas, S. L., Xu, S., Yue, J., Bossert, K., Becker, E., & Baumgarten, G. (2019). Characteristics of the quiet-time hot spot gravity waves observed by GOCE over the Southern Andes on 5 July 2010. *Journal of Geophysical Research: Space Physics*, *124*(8), 7034–7061. https://doi.org/10.1029/2019ja026693

Waldock, J., & Jones, T. (1986). HF Doppler observations of medium-scale travelling ionospheric disturbances at mid-latitudes. *Journal of Atmospheric and Terrestrial Physics*, *48*(3), 245–260. https://doi.org/10.1016/0021-9169(86)90099-1

Xu, S., Yue, J., Xue, X., Vadas, S. L., Miller, S. D., Azeem, I., et al. (2019). Dynamical coupling between Hurricane Matthew and the middle to upper atmosphere via gravity waves. *Journal of Geophysical Research: Space Physics*, *124*, 3589–3608. https://doi.org/10.1029/2018ja026453